Nano-Micro Letters

e-ISSN 2150-5551
CN 31-2103/TB

ARTICLE

https://doi.org/10.1007/s40820-026-02289-3

Cite as
Nano-Micro Lett.
(2026) 18:438

Received: 18 March 2026
Accepted: 20 June 2026


# Crystal Phase Engineering Accelerates Hydrogen Reverse Spillover for Efficient Alkaline Hydrogen Production

Jun Zhang[1], Xiaoyu Chen[2], Bin Wu[3] ✉, Xiangyang Guo[4], Xianlin Qu[5], Qunzhi Ma[1], Ying Wang[1], Jiayi Li[1], Wei Liu[1], Xu Li[1], Liyun Cao[1], Yi Wang[5], Jianfeng Huang[1] ✉, Jingxiang Zhao[2] ✉, Fuxiang Zhang[4] ✉, Yongqiang Feng[1] ✉

## HIGHLIGHTS

- Phase engineering of $ZrO_2$ regulates the electronic metal–support interactions and work function difference between Ru and $ZrO_2$, resulting in reverse hydrogen spillover, therefore enhancing electrocatalytic hydrogen evolution reaction in alkaline medium.
- The Ru@*m*-$ZrO_2$/C catalyst demonstrated a low overpotential and high mass activity (45 times that of commercial 20% Pt/C), and when integrated into an anion-exchange membrane water electrolyzer, it exhibited stable operation for over 300 hours.

**ABSTRACT** Phase engineering has proved effective in enhancing electrocatalytic performance by precisely controlling crystal structures. While significant efforts have been dedicated to phase regulation of active metals, the role of crystal phase of catalyst supports in steering the hydrogen migration during hydrogen evolution reaction (HER) remains underexplored. This work systematically investigates zirconium dioxide in its monoclinic (*m*-$ZrO_2$) and tetragonal (*t*-$ZrO_2$) phases as supports for Ru nanoclusters. A combination of spectroscopy and theoretical calculation demonstrates strong electronic metal–support interactions and work function difference between Ru and *m*-$ZrO_2$ lead to interfacial charge accumulation, accelerated water dissociation, and reverse hydrogen spillover, significantly enhancing electrocatalytic HER performance in alkaline medium. The Ru@*m*-$ZrO_2$/C catalyst exhibits excellent HER activity in different electrolytes. It achieves 10 mA $cm^{-2}$ with an extremely low overpotential ($\eta_{10}$) of only 28 mV in 1 M KOH, delivering a mass activity of 2.72 A $mg_{Ru}^{-1}$ (at 50 mV overpotential), which is 45 times higher than that of commercial Pt/C. The $\eta_{10}$ values are 56, 42, and 30 mV in 0.5 M $H_2SO_4$, 1 M KOH + 2 M NaCl, and 1 M KOH + simulated seawater, respectively. Furthermore, the catalyst also demonstrates excellent stability under alkaline simulated seawater electrolysis conditions. When integrated into an anion-exchange membrane water electrolyzer, it achieves 1.0 A $cm^{-2}$ at 1.76 V with stability exceeding 300 h. This work underscores the pivotal importance of support phase engineering for designing high-performance electrocatalysts for water splitting.

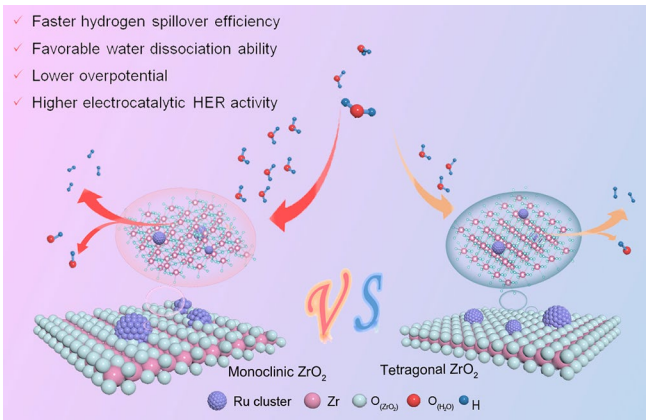


Jun Zhang, Xiaoyu Chen, and Bin Wu have contributed equally to this work.

✉ Bin Wu, bin.wu@ntu.edu.sg; Jianfeng Huang, huangjf@sust.edu.cn; Jingxiang Zhao, zhaojingxiang@hrbnu.edu.cn; Fuxiang Zhang, fxzhang@dicp.ac.cn; Yongqiang Feng, fengyq@sust.edu.cn

[1] Shaanxi Key Laboratory of Green Preparation and Functionalization for Inorganic Materials, School of Materials Science and Engineering, Shaanxi University of Science and Technology, Xi'an 710021, People's Republic of China

[2] College of Chemistry and Chemical Engineering, Harbin Normal University, Harbin 150025, People's Republic of China

[3] School of Materials Science and Engineering, Nanyang Technological University, Singapore 639798, Singapore

[4] State Key Laboratory of Catalysis, Dalian National Laboratory for Clean Energy, Chinese Academy of Sciences, Dalian Institute of Chemical Physics, Dalian 116023, People's Republic of China

[5] Center for Microscopy and Analysis, Nanjing University of Aeronautics and Astronautics, Nanjing 211106, People's Republic of China

Published online: 13 July 2026

Shanghai Jiao Tong University Press

Springer

**KEYWORDS** Phase engineering; Zirconium dioxide; Electrocatalyst; Hydrogen production; Seawater electrolysis

## 1 Introduction

Phase engineering of nanomaterials (PEN) has emerged as a powerful strategy for enhancing electrocatalytic performance by precisely controlling crystal phase structures, thereby offering new pathways toward efficient energy conversion systems, *e.g.*, hydrogen production from water/seawater splitting [1–9], nitrate reduction for ammonia synthesis [10, 11], and alcohol oxidation in fuel cell [12–14]. Up to now, substantial efforts have been devoted to phase regulation of active metals (*e.g.*, Ru, Pt) to optimize their electronic structure and surface adsorption behavior for reactions including the hydrogen evolution reaction (HER), oxygen evolution reaction (OER), and oxygen reduction reaction (ORR), *etc.* [15–22]. For instance, controlled synthesis of face-centered cubic (*fcc*) Ru and hexagonal close-packed (*hcp*) Rh nanostructures has demonstrated remarkable enhancements in activity and stability [23]. However, considerably less attention has been paid to the crystal phase engineering of catalyst supports—a critical factor that governs metal–support interactions and reaction mechanisms such as hydrogen (reverse) spillover.

Electronic metal–support interactions (EMSI) have been leveraged to modulate electronic properties and adsorption energetics at the interfaces, as exemplified in systems such as Pt/$MoS_2$ [24] and $La_2Sr_2PtO_{7+\delta}$ [25]. On the other hand, the work function difference ($\Delta\Phi$) between metal and support plays a critical role in determining the interfacial charge transfer and hydrogen migration [26, 27]. Several advanced catalyst systems, including Ru-$WO_{3-x}$ [28] and Ir/$HfO_2$@C [29], have been designed to exploit hydrogen spillover pathways. It is reported that the large $\Delta\Phi$ could result in charge accumulation and trap hydrogen species at the interface, thereby facilitating hydrogen reverse spillover (HRS) from the support to metal sites. In contrast, hydrogen spillover is defined as the process by which hydrogen species, after dissociation at the metal sites, migrate to the support [30–33]. However, the role of the support's crystal phase in regulating EMSI and HRS effects remains underexplored.

Among various support materials, zirconium dioxide ($ZrO_2$) exhibits great potential due to its polymorphic nature (monoclinic, tetragonal, cubic, and mixed phases), hydrophilicity, and chemical stability [34–36]. These features make $ZrO_2$ an ideal platform for studying the relationship between support crystal phase, metal–support interaction, and hydrogen spillover [37–39]. Although $ZrO_2$ has been employed in thermal catalysis and stabilization of single-atom catalysts, its application in electrocatalytic HER in alkaline seawater splitting—particularly with regard to the effect of $ZrO_2$ phase on HER activity—has rarely been systematically investigated.

In contrast with conventional EMSI studies that focus on the reconstruction of interfacial electronic structure, the current work highlights the urgent need to advance the fundamental understanding of how the crystal phase of catalyst supports influences the electronic structure of metal centers, modulates metal–support interactions, and directs HRS processes. Specifically, monoclinic $ZrO_2$ (*m*-$ZrO_2$) and tetragonal $ZrO_2$ (*t*-$ZrO_2$) supported Ru nanoclusters, defined separately as Ru@*m*-$ZrO_2$/C and Ru@*t*-$ZrO_2$/C, were successfully synthesized by a two-step solvothermal annealing process. Benefiting from the strong EMSI and large $\Delta\Phi$ between the surface Ru species and *m*-$ZrO_2$ support, the as-synthesized Ru@*m*-$ZrO_2$/C exhibits superior HER activity in different media. To deliver a current density of 10 mA $cm^{-2}$, it requires overpotential of 28, 56, 42, and 30 mV in 1 M KOH, 0.5 M $H_2SO_4$, 1 M KOH + 2 M NaCl, and 1 M KOH + simulated seawater, respectively. It also achieves a mass activity as high as 2.72 A $mg_{Ru}^{-1}$ at 50 mV overpotential in 1 M KOH, surpassing that of commercial 20% Pt/C by a factor of 45. In situ Raman, electrochemical impedance spectrum (EIS), and density functional theory (DFT) calculation results unveil that the charges accumulated at the Ru/*m*-$ZrO_2$ interface not only facilitate the water adsorption and dissociation process at Zr sites, but accelerate the reverse hydrogen spillover from *m*-$ZrO_2$ substrate to Ru sites by regulating the *d*-band center of Ru, thereby enhancing the electrocatalytic HER performance. Practically, Ru@*m*-$ZrO_2$/C also displays outstanding electrocatalytic activity toward direct seawater electrolysis for hydrogen production with high durability. When assembled in an anion-exchange membrane water electrolyzer (AEMWE) using Ru@*m*-$ZrO_2$/C as the cathode and NiFe-layered double hydroxide (NiFe-LDH) as the anode operating at 60 °C in 1 M KOH, a current density of 1.0 A $cm^{-2}$ is achieved at a cell voltage of 1.76 V, which can maintain stable for more than 300 h. This work aims to bridge the gap between phase-controlled support design and HRS-enhanced

 https://doi.org/10.1007/s40820-026-02289-3

catalysis, providing a fresh direction for the design of next-generation electrocatalysts for hydrogen production from water splitting.

## 2 Experimental Section

### 2.1 Materials

Zirconium chloride ($ZrCl_4$) was purchased from Shanghai Aladdin Biochemical Technology Co., Ltd. Terephthalic acid ($H_2BDC$) was purchased from Saen Chemical Technology (Shanghai) Co., Ltd. Formic acid (HCOOH) was purchased from Tianjin Kemiou Chemical Reagent Co., Ltd. Dimethyl-formamide (DMF) was purchased from Anhui Zesheng Technology Co., Ltd. Methanol (MeOH, $CH_3OH$), ethanol (EtOH, $CH_3CH_2OH$), and isopropyl alcohol (IPA, $C_3H_8O$) were purchased from Chemical Reagent Co., Ltd. Ruthenium (III) chloride anhydrous ($RuCl_3$), Pt/C (20 wt%), Ru/C (5 wt%), Nafion solution (5%), potassium thiocyanate (KSCN, 99%), ethylenediamine (EDTA, 99%), and potassium hydroxide (KOH, ≧85%) were purchased from Sigma-Aldrich. Sulfuric acid ($H_2SO_4$, 98.5%) was purchased from Codow (Guangdong, China). NaCl, $MgCl_2$, $MgSO_4$, $CaCl_2$, $NaHCO_3$, $Na_2SO_4$, and KCl were purchased from Tianjin Tianli Chemical Reagent Co., Ltd. Deionized water (DW, 18.25 MΩ $cm^{-1}$) was obtained from the ultrapure purification system (ULUPURE, UPDR-I-10 T). All the chemicals are analytical grade and used without further purification.

### 2.2 Preparation of Ru@*m*-$ZrO_2$/C, Ru@*t*-$ZrO_2$/C, and $ZrO_2$/C

#### 2.2.1 *Preparations of Ru@m-$ZrO_2$/C*

Ru@*m*-$ZrO_2$/C was synthesized by a two-step method [40, 41]. Firstly, a mixture of $ZrCl_4$ (240 mg), $H_2BDC$ (166.1 mg) and $RuCl_3$ (62.1 mg, 0.3 mmol) was dissolved in 55 mL of DMF containing 4 mL of HCOOH in a Teflon-lined autoclave and heated at 120 °C for 12 h. Then, the solid product was collected by washing with DMF and methanol and dried at 60 °C. The obtained product was labeled as Ru@UiO-66. Finally, the Ru@UiO-66 was annealed at 700 °C under Ar for 2 h to obtain Ru@*m*-$ZrO_2$/C. The cluster size (0.28, 0.31 and 0.34 mmol) and loading content (0.27, 0.29, 0.32 mmol) of Ru in Ru@*m*-$ZrO_2$/C were adjusted by alternating the addition amount of $RuCl_3$ while kept other procedures unchanged.

#### 2.2.2 *Preparations of Ru@t-$ZrO_2$/C and $ZrO_2$/C*

Ru@*t*-$ZrO_2$/C was synthesized by a three-step method. UiO-66 was synthesized in the same way as Ru@UiO-66, but without the addition of $RuCl_3$. Then, 0.3 mmol of $RuCl_3$ (62.1 mg) was introduced into a suspension of 200 mg of UiO-66 in 40 mL of methanol and stirred for 24 h. The obtained product, labeled as Ru/UiO-66, was collected by washing with methanol and dried at 60 °C. Finally, the Ru/UiO-66 was annealed at 700 °C under Ar for 2 h to obtain Ru@*t*-$ZrO_2$/C. For $ZrO_2$/C, the as-synthesized UiO-66 was directly annealed at 700 °C under Ar for 2 h. Similarly, the cluster size (0.28, 0.31, and 0.34 mmol) and loading content (0.29 and 0.32 mmol) of Ru in Ru@*t*-$ZrO_2$/C were adjusted by alternating the addition amount of $RuCl_3$.

### 2.3 Material Characterization

X-ray diffraction (XRD) patterns were obtained on a Rigaku D/max-2200PC diffractometer (Japan) with Cu Kα radiation. High-resolution transmission electron microscope (HR-TEM) measurement was conducted on a JEOL JEM-2010F with a 200 kV acceleration voltage. Aberration-corrected high-angle annular dark-field scanning transmission electron microscopy (AC-HAADF-STEM) measurement was conducted on a Thermo Fisher Scientific Spectra 300 operating at 300 kV with cold field emission gun. Raman spectroscopy analysis was performed on a Renishaw-invia microscopic confocal laser Raman spectrometer with a 532-nm laser. Fourier transform infrared spectroscopy (FT-IR) was carried out on a Nicolet-5700 spectrometer in the range of 4000–100 $cm^{-1}$. Scanning electron microscope (SEM) measurement was taken on a Hitachi S-4800 microscope. X-ray photoelectron spectroscopy (XPS) was collected on a Thermo Scientific ESCA Lab 250Xi with Al Kα radiation (200 W). Inductively coupled plasma atomic emission spectroscopy (ICP-AES) measurement was conducted on a SHIMADZU ICPE-90000 instrument. The electrochemical performance was tested on a CHI660E workstation (Chenhua, Shanghai).

### 2.4 Synchrotron Radiation X-ray Absorption Spectrum Measurement

X-ray absorption near edge structure (XANES) and extended X-ray absorption fine structure (EXAFS) were collected on the BL14W1 beamline in Shanghai Synchrotron Radiation Facility (SSRF). The energy was calibrated by a Ru foil for the Ru K-edge. All data were obtained at room temperature.

### 2.5 In Situ Electrochemical Raman Measurements

The in situ Raman was performed on a RTS2-DZ-A using a 532-nm laser. During tests, the Ag/AgCl electrode was used as the reference electrode (RE), the platinum wire served as the counter electrode (CE), and the catalyst was loaded on the Ti mesh as the working electrode (WE). Raman spectroscopy was obtained at a voltage of OCP, 0, − 0.005, − 0.010, − 0.015, and − 0.020 V versus reversible hydrogen electrode (RHE) and without voltage. After 100 s of constant voltage stabilization, each spectrum was collected.

### 2.6 Electrochemical Measurement

All the electrochemical measurements were conducted on a CHI660E electrochemical workstation by a three-electrode system. The 1 M KOH and 0.5 M $H_2SO_4$ electrolyte solutions were prepared from 98% concentrated $H_2SO_4$ and KOH solid and ultrapure water, respectively. The 1 M KOH: *x* M NaCl (*x* = 0, 0.5, 2) electrolyte solution was prepared by KOH and NaCl solid and ultrapure water, and the pH values were 13.99, 13.94, and 13.77 [42], respectively. For the simulated seawater, firstly a mixture of 26.73 g of NaCl, 2.26 g of $MgCl_2$, 3.25 g of $MgSO_4$, 1.12 g of $CaCl_2$, 0.19 g of $NaHCO_3$, 3.48 g of $Na_2SO_4$, and 0.72 g of KCl was dissolved into 1.0 L of ultrapure water [29]. Then, an equal volume of 1 M KOH and the above simulated seawater was mixed and centrifuged to obtain the supernatant as alkaline simulated seawater. The pH value of alkaline simulated seawater was 13.96. A glass carbon electrode (GCE, $\phi = 3$ mm), a graphitic rod, a Hg/HgO for alkaline and Ag/AgCl for acidic conditions were used as the working, counter- and reference electrode, respectively. To prepare the working electrode: Firstly, 10 mg of the catalyst was dispersed in 195 μL of IPA containing 5 μL of Nafion solution through ultrasonication. Then, 2 μL of the ink was dripped on the surface of GCE and dried at room temperature. All potentials reported in this work were calibrated to the RHE according to the Nernst equation:

E (RHE) = E (Hg/HgO) + 0.924 (1 M KOH).

E (RHE) = E (Ag/AgCl) + 0.281 (0.5 M $H_2SO_4$).

Linear sweep voltammetry (LSV) was performed with compensation at a scan rate of 1 mV $s^{-1}$. Tafel slopes were obtained from the LSV curves according to the equation of $\eta = a + b \lg j$, where $\eta$ refers to the overpotential, b is the Tafel slope, and a denotes the intercept [43]. The electrochemically active surface area (ECSA) and double-layer capacitor ($C_{dl}$) can be obtained in the non-Faradaic region by cyclic voltammetry (CV) scanning with varied scan rate of 2, 4, 6, 8, 10, and 12 mV $s^{-1}$[44]. Faradic efficiency was measured using the drainage method under constant current condition. The electrochemical stability of catalysts was tested by chronoamperometry method at a constant potential. The turnover of frequency (TOF) was estimated by TOF = *I*/2Fn [45], where *I* refers to measured hydrogen current (A), F is Faradaic constant (96,485 C $mol^{-1}$), n is amount of active sites (mol) obtained by the CO-stripping method ($n = Q_{CO}/2F$). The mass activity (MA) is calculated based on the following equation: MA = *I*/*m*, where *I* (A) is the measured current and m (mg) is the mass of Ru loaded on a glassy carbon electrode [29].

### 2.7 AEMWE Device Test

The anion-exchange membrane (AEM) was prepared by sandwiching the cathodes and anodes on both sides of the membrane (Fumasep FAA-3-PK-130, 110–130 μm thickness). The catalyst of Ru@*m*-$ZrO_2$/C loaded on gas diffusion layer (Ru@*m*-$ZrO_2$/C/GDL) and NiFe-LDH/GDL (Cropping area: 2.5 × 2.5 $cm^2$, active area: 1 × 1 $cm^2$, loading: 6.0 mg $cm^{-2}$) were used as cathode and anode, respectively. Subsequently, the AEMWE system was filled with 1.0 M KOH electrolyte, and the flow rate was controlled at 40 mL $min^{-1}$ using a peristaltic pump. Following this, the performance of the AEMWE was assessed with DC power supply. The


https://doi.org/10.1007/s40820-026-02289-3

long-term stability of the device was evaluated using the chronopotentiometry method.

### 2.8 Theoretical Section

All spin-polarized DFT computations were carried out using the Vienna Ab initio Simulation Package (VASP) [46]. The Perdew–Burke–Ernzerhof (PBE) functional within the generalized gradient approximation (GGA) was employed to describe the exchange–correlation potential [47], using a plane-wave energy cutoff of 450 eV. Consistent with our experimental observations, the (111) and (101) facets were constructed for monoclinic and tetragonal $ZrO_2$ materials, denoted as *m*-$ZrO_2$ and *t*-$ZrO_2$, respectively. To simulate the sub-nanometer Ru particles observed experimentally, we anchored $Ru_5$ cluster onto *m*-$ZrO_2$ and *t*-$ZrO_2$, with the upper two substrate layers fully optimized and the bottom two layers fixed. A vacuum space of 30 Å was applied along the z-direction to minimize interactions between periodic images. Γ-point sampling was performed with a $3\times3\times1$ k-point grid. The energy convergence criterion was set to $10^{-5}$ eV, and ionic relaxations were conducted until the maximum force on each atom fell below 0.03 eV $Å^{-1}$. van der Waals interactions were accounted for using the DFT-D3 method, and transition states were located using the climbing image nudged elastic band (CI-NEB) method [48].

To evaluate the catalytic activity toward the HER, the free energy change was computed as $\Delta G = \Delta E + \Delta ZPE - T\Delta S$ [49, 50], where ΔE represents the reaction energy from the DFT computations. ΔZPE and TΔS are the energy changes in the zero-point energy and entropy at 298.15, respectively, obtained from vibrational frequency computations and the NIST database for isolated $H_2$ and $H_2O$. In the HER, the closer the Gibbs free energy of the key intermediate $H^*$ ($\Delta G_{H^*}$) is to zero, the better the catalytic performance of the surface catalyst [51, 52].

## 3 Results and Discussion

### 3.1 Synthesis and Structure Characterization

The Ru@*m*-$ZrO_2$/C was prepared via a solvothermal annealing process as displayed in Fig. 1a. Typically, $RuCl_3$ was introduced into the precursor solution containing $H_2BDC$ and $ZrCl_4$ to form a porous metal–organic framework (defined as Ru@UiO-66, Figs. S1–S4), which was then annealed at 700 °C under Ar atmosphere, converting UiO-66 to monoclinic $ZrO_2$ (Figs. S5–S7). In contrast, post-impregnation of $RuCl_3$ into pre-synthesized UiO-66 (denoted as Ru/UiO-66) results in reduction to tetragonal $ZrO_2$ during annealing, thereby forming the Ru@*t*-$ZrO_2$/C counterpart. The crystal phases of Ru@*m*-$ZrO_2$/C and Ru@*t*-$ZrO_2$/C are first confirmed by XRD. Although the precursor of Ru@UiO-66 and Ru/UiO-66 exhibits similar morphology and structure (Figs. S1–S4), the thermal reduction treatment generates distinct crystalline architectures. As shown in Fig. 1b, a monoclinic $ZrO_2$, featuring with 2θ positions at 24.1°, 28.2°, 31.5°, 34.2°, 35.2°, 49.3°, and 50.2°, which are well indexed to the (011), (− 111), (111), (002), (200), (022), and (220) planes of monoclinic zirconia (JCPDS#83-0936), respectively, is observed in Ru@*m*-$ZrO_2$/C, while the XRD pattern of Ru@*t*-$ZrO_2$/C reassembles the pristine $ZrO_2$/C, characterized by a set of diffraction peaks at 30.2°, 35.3°, 50.3°, and 60.2°, corresponding to the (101), (110), (112), and (211) facets of tetragonal zirconia (JCPDS#79-1770), respectively. In both cases, no signal from Ru nanoparticles is detected, indicative of atomic dispersion of Ru species on $ZrO_2$ support [53]. The strong adsorption peaks at 742, 584, and 507 $cm^{-1}$ in the FT-IR spectroscopy [54] (Fig. S6) and 185, 331, 375 $cm^{-1}$ in the Raman spectrum [55, 56] (Fig. S7) of Ru@*m*-$ZrO_2$/C further demonstrated the existence of *m*-$ZrO_2$.

The morphology and structure of Ru@*m*-$ZrO_2$/C and Ru@*t*-$ZrO_2$/C are then investigated by TEM. The high-resolution TEM, high-angle annular dark-field scanning transmission electron microscopy (HAADF-STEM) images (Figs. S8–S13) and corresponding HAADF image with false color (Fig. 1c, g) show that some bright nanoclusters with diameter of 1–2 nm are anchored on the large nanoparticles and dispersed on the carbon substrate in Ru@*m*-$ZrO_2$/C and Ru@*t*-$ZrO_2$/C. Aberration-corrected HAADF-STEM further reveals the lattice distance of 0.265 and 0.305 nm assigned to the (002) facet of *m*-$ZrO_2$ and (101) of *t*-$ZrO_2$ (Fig. 1d, f, h), respectively. The slightly larger crystal spacing of $ZrO_2$ substrate in Ru@*m*-$ZrO_2$/C and Ru@*t*-$ZrO_2$/C with respect to the parent *m*-$ZrO_2$ and *t*-$ZrO_2$ could be caused by the formation of Ru–O–Zr connection after loading of Ru clusters. The corresponding fast Fourier transform (FFT) patterns in the square region marked by pink and blue dotted lines for Ru@*m*-$ZrO_2$/C (Fig. 1e) and Ru@*t*-$ZrO_2$/C (Fig. 1i) confirm

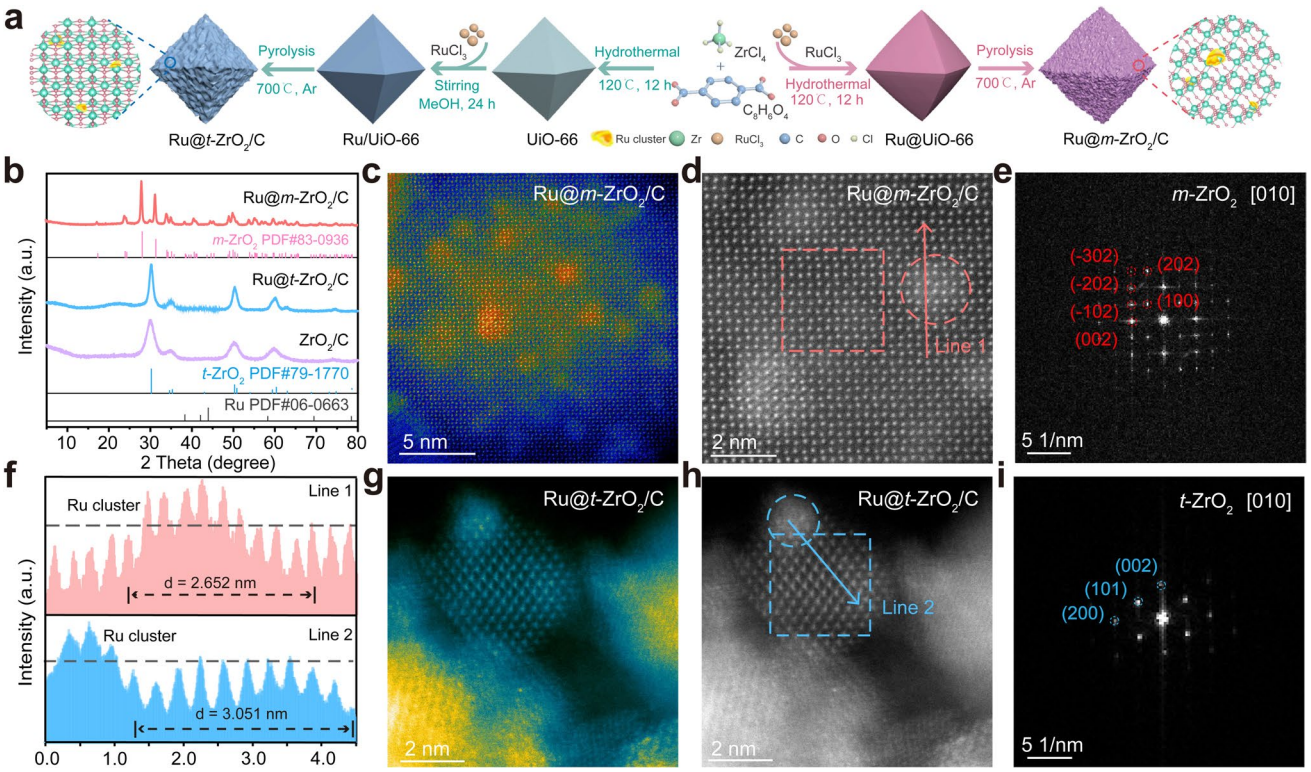


**Fig. 1** Crystal phase structural characterization. **a** Schematic illustration of the synthetic route of Ru@*m*-$ZrO_2$/C and Ru@*t*-$ZrO_2$/C. **b** XRD patterns of Ru@*m*-$ZrO_2$/C, Ru@*t*-$ZrO_2$/C, and $ZrO_2$/C. **c** False-color HAADF-STEM image, **d** aberration-corrected HAADF-STEM of Ru@*m*-$ZrO_2$/C and **e** the corresponding FFT pattern along the [010] zone axis from the pink dotted square in (**d**). **f** Line intensity profiles of the pink and blue arrows in (**d**) and (**h**) for Ru@*m*-$ZrO_2$/C and Ru@*t*-$ZrO_2$/C, respectively. **g** False-color HAADF-STEM image, **h** aberration-corrected HAADF-STEM of Ru@*t*-$ZrO_2$/C and **i** the corresponding FFT pattern along the [010] zone axis from the blue dotted square in (**h**)

the $ZrO_2$ along [010] zone axes, respectively [57]. The line intensity profiles at the pink and blue arrows separately for Ru@*m*-$ZrO_2$/C and Ru@*t*-$ZrO_2$/C ambiguously demonstrate the successful incorporation of Ru cluster on the $ZrO_2$ matrix (Fig. 1f). The corresponding energy-dispersive X-ray spectroscopy (EDS) mapping reveals the homogeneous distribution of Zr, O, and C elements and the Ru clusters on the $ZrO_2$ support (Figs. S12a and S14). Based on the ICP-AES, the Ru content in Ru@*m*-$ZrO_2$/C and Ru@*t*-$ZrO_2$/C is 0.72 and 1.02 wt%, respectively (Table S1).

The chemical valence state and local coordination structure of $ZrO_2$ support and Ru species in Ru@*m*-$ZrO_2$/C and Ru@*t*-$ZrO_2$/C are unveiled by XAS and XPS. As shown in Figs. 2a and S15, the typical feature at 18,014 eV in the Zr K-edge XANES spectroscopy proves the $Zr^{4+}$ valence state in Ru@*m*-$ZrO_2$/C and Ru@*t*-$ZrO_2$/C [58]. Fourier-transformed extended X-ray absorption fine structure (FT-EXAFS) spectroscopy (Fig. 2b) and fitting curves (Fig. S16) disclosed two distinctive geometry of $ZrO_2$ in Ru@*m*-$ZrO_2$/C and Ru@*t*-$ZrO_2$/C [59, 60]. For the former, the peak at 1.58 and 3.0 Å is assigned to Zr–O and Zr–Zr shell with coordination number (CN) of 8 and 6 (Table S2), respectively [58], while the Zr–O and Zr–Zr scattering in Ru@*t*-$ZrO_2$/C was located separately at 1.50 and 3.2 Å with CN of 4 and 12, respectively [61]. Such coordination environment divergence is also reflected by the wavelet transform (WT) of EXAFS at Zr K-edge for Ru@*m*-$ZrO_2$/C and Ru@*t*-$ZrO_2$/C (Fig. S17). Figure 2c illustrates the Ru K-edge XANES, of which the adsorption edge of Ru@*m*-$ZrO_2$/C and Ru@*t*-$ZrO_2$/C locates between those of Ru foil and $RuO_2$ references, indicative of valence state of Ru in the range of 0 ~ 4. The first derivative XANES spectra further demonstrate a relatively higher valence state of Ru in Ru@*m*-$ZrO_2$/C with respect to Ru@*t*-$ZrO_2$/C (Fig. S18). The FT-EXAFS (Fig. 2d) and fitting result (Fig. S19 and Table S3) reveals the formation of Ru–O and Ru–Ru bond in Ru@*m*-$ZrO_2$/C with CN of 2.7 and 2.5, respectively,


https://doi.org/10.1007/s40820-026-02289-3

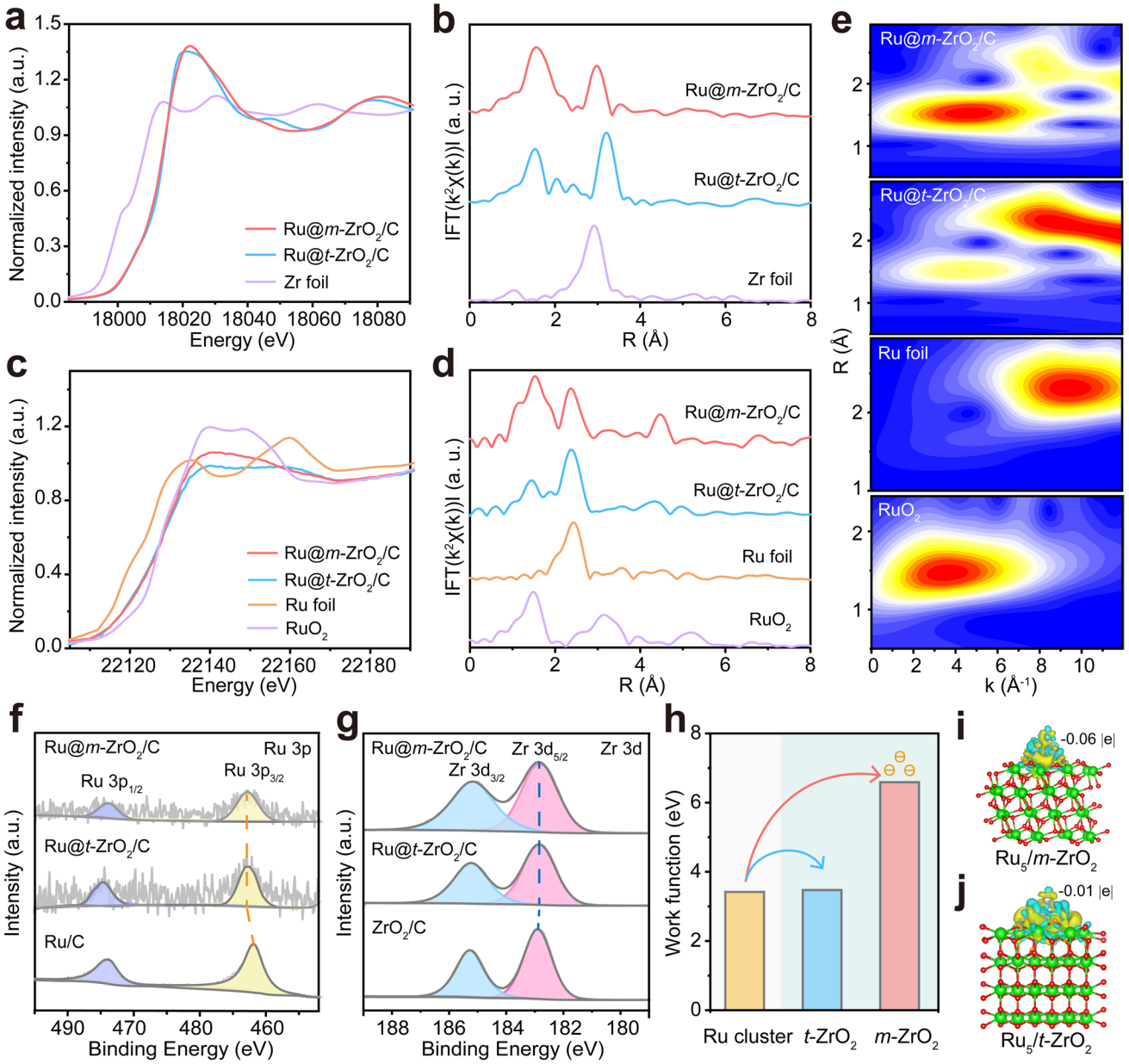


**Fig. 2** Electronic and coordination structure characterization. **a** Zr K-edge XANES spectra and **b** FT-EXAFS spectra of Ru@*m*-$ZrO_2$/C, Ru@*t*-$ZrO_2$/C and Zr foil. **c** Ru K-edge XANES spectra, **d** FT-EXAFS spectra, and **e** the corresponding wavelet transform images of Ru@*m*-$ZrO_2$/C, Ru@*t*-$ZrO_2$/C, Ru foil and $RuO_2$. **f** Ru 3*p* XPS profiles of Ru@*m*-$ZrO_2$/C, Ru@*t*-$ZrO_2$/C and Ru/C. **g** Zr 3*d* XPS profiles of Ru@*m*-$ZrO_2$/C, Ru@*t*-$ZrO_2$/C and $ZrO_2$/C. **h** Work function of Ru cluster, *m*-$ZrO_2$ and *t*-$ZrO_2$. Charge density difference images of **i** Ru@*m*-$ZrO_2$/C, and **j** Ru@*t*-$ZrO_2$/C. Color code for the balls: Zr, green; O, red; Ru, cyan. The blue and yellow contour part represents charge depletion and accumulation, respectively

which is further confirmed by WT-EXAFS at Ru K-edge for Ru@*m*-$ZrO_2$/C and Ru@*t*-$ZrO_2$/C (Fig. 2e).

The electronic structure of Ru@*m*-$ZrO_2$/C and Ru@*t*-$ZrO_2$/C was also revealed by XPS. The Ru 3*p* XPS spectrum (462.87 eV for Ru $3p_{3/2}$ and 483.97 eV for Ru $3p_{1/2}$) of Ru@*m*-$ZrO_2$/C and Ru@*t*-$ZrO_2$/C displayed a upshift to higher binding energy (BE) with respect to Ru/C (Figs. 2f and S20–S22), while the BEs for Zr 3*d* down-shift relative to $ZrO_2$/C (Fig. 2g). The result indicates that the electrons transfer from Ru sites to $ZrO_2$ substrate via Ru–O–Zr path,

which was further confirmed by the work function (WF) and charge density difference (CDD) calculation. As shown in Fig. 2h, the *m*-$ZrO_2$ possesses a much larger WF (6.59 eV) than those of *t*-$ZrO_2$ (3.47 eV) and Ru cluster (3.42 eV). The larger $\Delta\Phi$ between Ru cluster and *m*-$ZrO_2$ substrate could drive electrons accumulation at the Ru/*m*-$ZrO_2$ interface, facilitating the adsorption of water molecules. CDD diagrams and Bader charge analysis (Fig. 2i, j) further illustrate more charge depletion from the $Ru_5$ cluster to *m*-$ZrO_2$ (0.06 e) with respect to *t*-$ZrO_2$ (0.01 e).

### 3.2 Electrocatalytic HER Performance

The HER catalytic performance of Ru@*m*-$ZrO_2$/C and Ru@*t*-$ZrO_2$/C was evaluated in a three-electrode system with 1 M KOH electrolyte. For comparison, Pt/C, Ru/C, and $ZrO_2$/C were selected as references. As shown in Fig. 3a, b, Ru@*m*-$ZrO_2$/C exhibits the lowest overpotential, requiring only 28 mV to reach 10 mA $cm^{-2}$, outperforming Ru@*t*-$ZrO_2$/C (35 mV), Pt/C (36 mV), Ru/C (48 mV), and $ZrO_2$/C (716 mV). The corresponding Tafel slopes (Fig. 3c) further reveal the HER kinetics, with values of 31.4, 42.2, 51.0, 69.9, and 203.0 mV $dec^{-1}$ for Ru@*m*-$ZrO_2$/C, Ru@*t*-$ZrO_2$/C, Pt/C, Ru/C, and $ZrO_2$/C, respectively, indicating superior reaction kinetics for Ru@*m*-$ZrO_2$/C [62, 63]. Furthermore, control experiments demonstrate the cluster size and dispersion of Ru clusters in Ru@*m*-$ZrO_2$/C and Ru@*m*-$ZrO_2$/C have negligible effect on the catalytic HER performance (Figs. S23–S26 and Tables S4 and S5). To probe the intrinsic activity, TOF was measured based on CO-stripping experiment [45]. The results (Figs. 4d and S27, Table S6) confirm that Ru@*m*-$ZrO_2$/C exhibits a high TOF value. Mass activity (MA) of Ru@*m*-$ZrO_2$/C at $\eta_{50}$ was as large as 2.72 A $mg_{Ru}^{-1}$ (Fig. S28), 45-fold higher than that of commercial 20% Pt/C. ECSA estimated via $C_{dl}$ from CV measurements (Fig. S29) [64] is highest for Ru@*m*-$ZrO_2$/C at 37.6 mF $cm^{-2}$, compared to 20.2 mF $cm^{-2}$ for Ru@*t*-$ZrO_2$/C, 16.6 mF $cm^{-2}$ for Pt/C, and 4.7 mF $cm^{-2}$ for $ZrO_2$/C. Moreover, the charge transfer resistance ($R_{ct}$) is derived from EIS data (Fig. S30) [65], of which Ru@*m*-$ZrO_2$/C exhibits a smallest $R_{ct}$ value, indicative of favorable charge transfer kinetics of Ru@*m*-$ZrO_2$/C. In addition, the Faradaic efficiency of Ru@*m*-$ZrO_2$/C was measured to be approximately 96.8% (Fig. 3e). The HER parameters of Ru@*m*-$ZrO_2$/C are comparably listed in Fig. 3f and Table S7, evidently confirming the superior performance among all the samples. To elucidate the nature of active sites, poisoning experiments using EDTA and KSCN are conducted (Fig. S31). The significant decrease in current density upon KSCN addition—contrasting with negligible change after EDTA treatment—suggests that Ru species primarily exist as clusters, which are critical for HER activity [66]. The Ru@*m*-$ZrO_2$/C catalyst also exhibited exceptional stability in alkaline medium, maintaining performance over 100 h at 100 mA $cm^{-2}$ (Fig. 3g). Moreover, after 5000 cycles of continuous CV scanning, the LSV curve of Ru@*m*-$ZrO_2$/C almost overlapped with the initial one, further demonstrating the robust durability. Notably, Ru@*m*-$ZrO_2$/C also demonstrated enhanced activity in acidic medium, requiring a $\eta_{10}$ of 56 mV, a Tafel slope of 49.4 mV $dec^{-1}$, and a $C_{dl}$ value of 30.3 mF $cm^{-2}$ (Figs. S32 and S33). Moreover, post-test analyses via XRD, Raman, SEM, and XPS confirmed the structural and chemical stability of Ru@*m*-$ZrO_2$/C (Figs. S34–S39). In addition, the HER performance of Ru@*m*-$ZrO_2$/C surpasses many reported electrocatalysts (Fig. 3h, Tables S8 and S9).

### 3.3 Experimental Evidence for Hydrogen Reverse Spillover

To elucidate the underlying mechanism for the enhanced HER activity of Ru@*m*-$ZrO_2$/C, various in situ/operando measurements were employed. Firstly, in situ Raman spectra of Ru@*m*-$ZrO_2$/C, Ru@*t*-$ZrO_2$/C, $ZrO_2$/C, and Ru/C were collected between 0 and − 0.02 V versus RHE (Figs. 4a–c and S40). At open-circuit potential (OCP), all samples only exhibit the typical D and G bands of carbon, which remained almost unchanged with decreasing potential, indicating that the carbon support does not participate in hydrogen migration [67]. Notably, as the potential becomes more negative, the Raman peaks of Ru@*m*-$ZrO_2$/C at 1118 and 1504 $cm^{-1}$ intensified more significantly than those of Ru@*t*-$ZrO_2$/C, while the corresponding signals for $ZrO_2$/C are rather weak and almost undetectable for Ru/C. To assign these peaks, the electrolyte was switched from KOH/$H_2O$ to KOD/$D_2O$ (Figs. 4a–c and S41). The peak at 1504 $cm^{-1}$ blue-shifts to 1468 $cm^{-1}$, and the peak at 1118 $cm^{-1}$ red-shifts to 1183 $cm^{-1}$ due to the H–D isotope effect, confirming that both peaks originate from hydrogen atom vibrations. These shifts allow assignment of the 1118 and 1504 $cm^{-1}$ bands to Zr–OH species at the Ru/$ZrO_2$ interface. Under $D_2O$ conditions, slower O–D bond cleavage leads to accumulation of detectable Ru-D species at ~ 876 $cm^{-1}$, providing clear HRS


https://doi.org/10.1007/s40820-026-02289-3

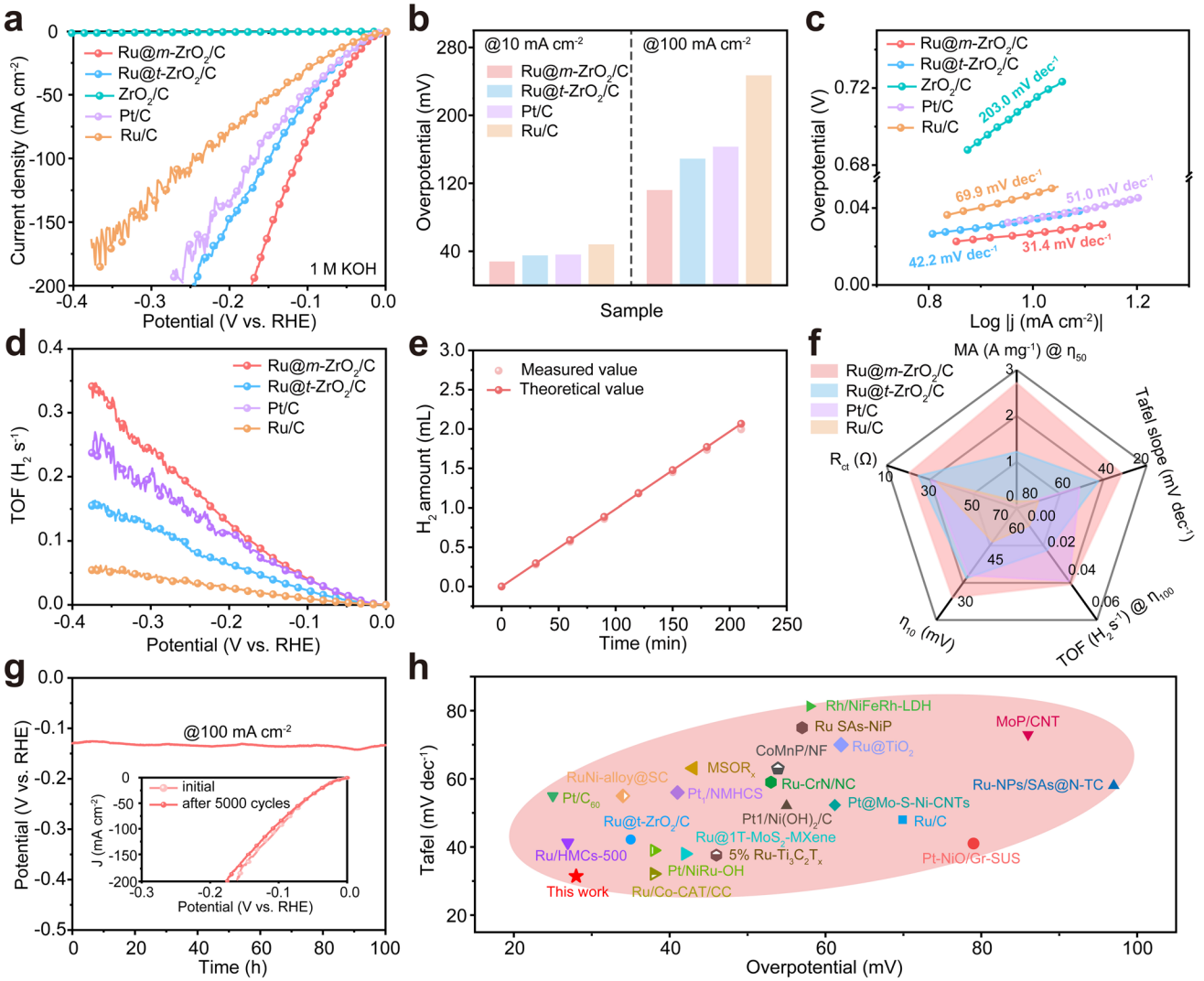


**Fig. 3** Electrocatalytic HER performance in 1 M KOH. **a** LSV curves, **b** overpotentials at 10 and 100 mA $cm^{-2}$, **c** Tafel slopes, and **d** TOF values for Ru@*m*-$ZrO_2$/C, Ru@*t*-$ZrO_2$/C, Pt/C and Ru/C. **e** Faradaic efficiency of Ru@*m*-$ZrO_2$/C. **f** Comparison of MA, $R_{ct}$, $\eta_{10}$, TOF and Tafel slope for Ru@*m*-$ZrO_2$/C, Ru@*t*-$ZrO_2$/C, Pt/C and Ru/C. **g** Chronopotentiometry curve of Ru@*m*-$ZrO_2$/C at 100 mA $cm^{-2}$, inset showing the LSV curve before and after 5000 cycles of CV scanning. **h** Comparison of HER performance of Ru@*m*-$ZrO_2$/C with the recently-reported HER electrocatalysts

evidence of H* migration from $ZrO_2$ support to Ru sites. Compared with Ru@*t*-$ZrO_2$/C, Ru@*m*-$ZrO_2$/C exhibits a stronger Ru–D signal, further demonstrating the enhanced OH adsorption capacity and superior water dissociation ability of the *m*-$ZrO_2$ support. Additionally, CO-stripping measurements were conducted to evaluate OH adsorption ability of Ru@*m*-$ZrO_2$/C (Fig. S42), as CO oxidation requires reactive OH* species [68]. In CO-saturated 1 M KOH electrolyte, the onset potential for CO oxidation over Ru@*m*-$ZrO_2$/C is negatively shifted by ~73 mV compared to Ru@*t*-$ZrO_2$/C, indicating more facile OH adsorption on the Ru@*m*-$ZrO_2$/C surface due to strong Ru/*m*-$ZrO_2$ EMSI effect.

Furthermore, the EMSI effect enables to induce interfacial electric field polarization, which is critical in regulation of hydrogen-bond network rearrangement within the electric double layer (EDL). Using Gaussian fitting, the broad peak between 3000 and 3800 $cm^{-1}$ in the Raman spectra of Ru@*m*-$ZrO_2$/C and Ru@*t*-$ZrO_2$/C (Fig. 4d), attributed to interfacial water vibrations, could be deconvoluted into three components: four-coordinated hydrogen-bonded water (4-HB·$H_2O$), two-coordinated hydrogen-bonded water

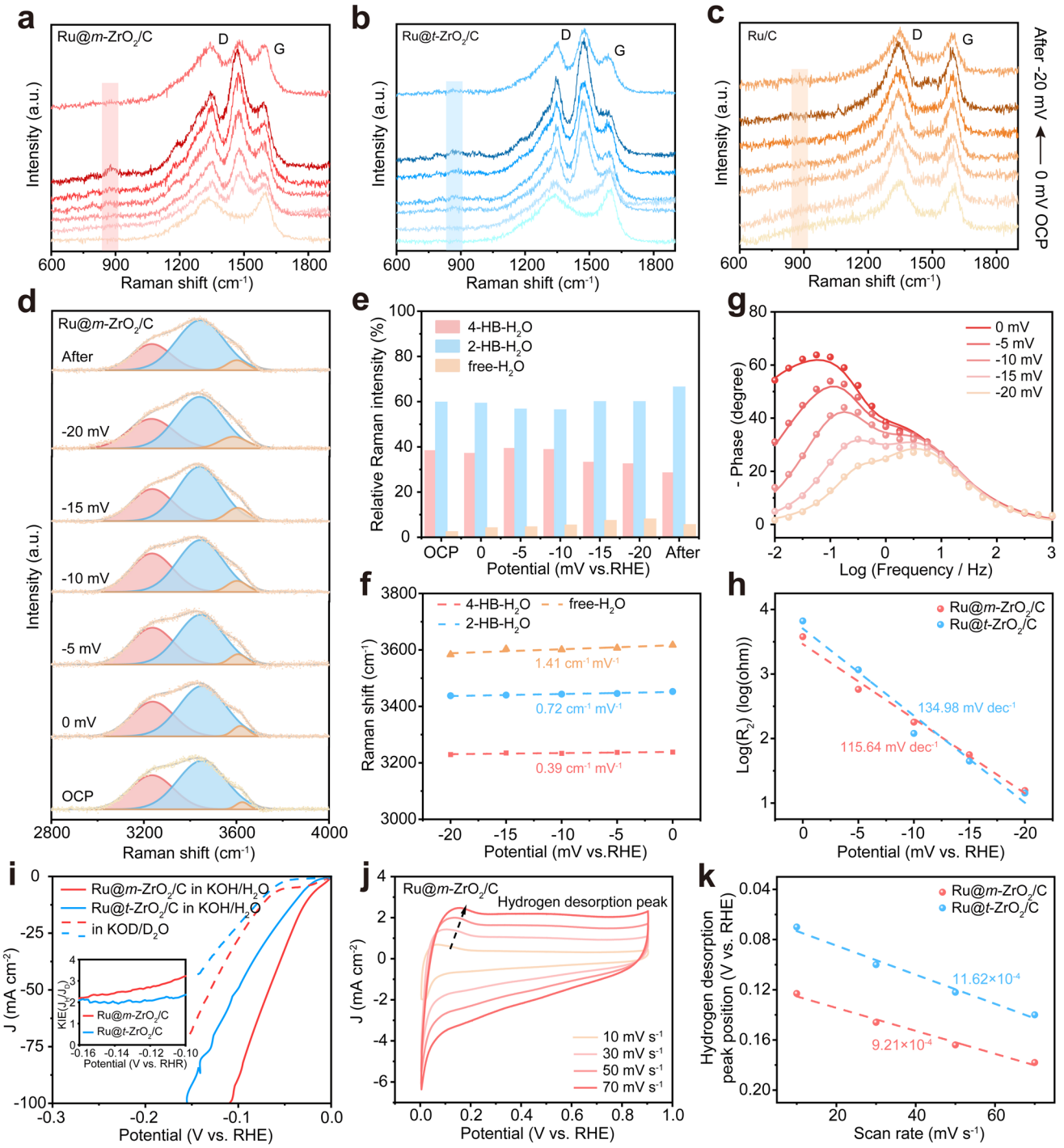


**Fig. 4** Experimental insights on HER mechanism. In situ Raman spectra of **a** Ru@*m*-$ZrO_2$/C, **b** Ru@*t*-$ZrO_2$/C and **c** Ru/C in KOD/$D_2O$. **d** In situ Raman spectra of Ru@*m*-$ZrO_2$/C in the range of 2800–4000 $cm^{-1}$. **e** Population of 4-HB·$H_2O$, 2-HB·$H_2O$ and free $H_2O$, and **f** Stark slope derived from Raman spectra at different applied potential in (**d**). **g** Bode plots of Ru@*m*-$ZrO_2$/C at varied potentials, **h** Tafel slope of Ru@*m*-$ZrO_2$/C and Ru@*t*-$ZrO_2$/C estimated from $R_2$. **i** Polarization curves of Ru@*m*-$ZrO_2$/C and Ru@*t*-$ZrO_2$/C in 1 M KOH/$H_2O$ (solid lines) and KOD/$D_2O$ (dashed lines), inset showing the KIE value against potential. **j** CV curves of Ru@*m*-$ZrO_2$/C. **k** Plots of hydrogen desorption peak position versus scan rate for Ru@*m*-$ZrO_2$/C and Ru@*t*-$ZrO_2$/C


https://doi.org/10.1007/s40820-026-02289-3

(2-HB·$H_2O$), and free $H_2O$ [69]. As depicted in Fig. 4e, the proportion of free $H_2O$ in Ru@*m*-$ZrO_2$/C is slightly higher than that in Ru@*t*-$ZrO_2$/C and increases rapidly with decreased potential (Figs. S43 and S44), indicating the interfacial free $H_2O$ in the EDL is critical for the hydrogen migration, contributing to the faster water dissociation kinetics over Ru@*m*-$ZrO_2$/C during HER [70, 71]. The trend for the vibrational frequency change along with the applied potential is attributed to the vibrational Stark effect [27, 72]. As shown in Fig. 4f, the Stark slope of free $H_2O$ (1.41 $cm^{-1}$ $mV^{-1}$) on Ru@*m*-$ZrO_2$/C is higher than those of 4-HB·$H_2O$ (0.39 $cm^{-1}$ $mV^{-1}$) and 2-HB·$H_2O$ (0.72 $cm^{-1}$ $mV^{-1}$) and also higher than that of Ru@*t*-$ZrO_2$/C (Fig. S43), indicating that free water on Ru@*m*-$ZrO_2$/C is more sensitive to the electrode's local electric field.

The hydrogen adsorption/desorption kinetics during water dissociation process were subsequently analyzed via in situ EIS measurement [67, 73]. The HER equivalent circuit model consists of three components (Fig. S45): $R_s$ represents the uncompensated solution resistance, while $CPE_1$ and $R_1$ correspond to the capacitance and resistance of hydrogen adsorption at low frequencies (Volmer step), and $CPE_2$ and $R_2$ represent hydrogen adsorption behavior on the catalyst surface at high frequencies (Heyrovsky step). Nyquist plots of Ru@*m*-$ZrO_2$/C and Ru@*t*-$ZrO_2$/C obtained at various overpotentials in alkaline medium are shown in Fig. S46 and Tables S10, S11. The corresponding Bode plots in Fig. 4g show two distinct phase angles, confirming that the HER process follows the Volmer–Heyrovsky mechanism. The rapid decrease in phase angles in the low-frequency region suggests fast water dissociation kinetics [74]. The hydrogen adsorption kinetics were quantified by fitting the logarithmic hydrogen adsorption resistance Log($R_2$) against overpotential [26]. As illustrated in Fig. 4h, Ru@*m*-$ZrO_2$/C exhibited a lower Tafel slope (115.64 mV $dec^{-1}$) than Ru@*t*-$ZrO_2$/C (134.98 mV $dec^{-1}$), indicating accelerated hydrogen adsorption and transfer over *m*-$ZrO_2$. The H/D kinetic isotope effect (KIE) is used to probe hydrogen/proton transfer kinetics [75]. Polarization curves revealed significantly lower HER activities for both catalysts in 1 M KOD/$D_2O$ compared to 1 M KOH/$H_2O$ (Fig. 4i), with KIE values exceeding 2, confirming the involvement of hydrogen/proton transfer in the HER process. Hydrogen desorption kinetics were further evaluated via CV measurement. By analyzing the shift in hydrogen desorption peak positions with varying scan rates (Figs. 4j, k and S47), the desorption kinetics were quantified [25]. The slope for Ru@*m*-$ZrO_2$/C ($9.21\times10^{-4}$) is lower than that for Ru@*t*-$ZrO_2$/C ($11.62\times10^{-4}$) in alkaline electrolyte, indicating faster hydrogen desorption on Ru@*m*-$ZrO_2$/C. In situ EIS and CV measurements under acidic conditions also demonstrated superior hydrogen adsorption/desorption kinetics for Ru@*m*-$ZrO_2$/C (Figs. S48–S51 and Tables S12 and S13).

### 3.4 Theoretical Insight into the Electrocatalytic Mechanism

To further elucidate the catalytic mechanism underlying the excellent HER activity of sub-nanometer Ru clusters anchored on $ZrO_2$ surfaces under alkaline conditions, DFT calculations were then performed. A $Ru_5$ cluster bonded on *m*-$ZrO_2$ ($Ru_5$/*m*-$ZrO_2$) and *t*-$ZrO_2$ ($Ru_5$/*t*-$ZrO_2$) was constructed to represent Ru@*m*-$ZrO_2$/C and Ru@*t*-$ZrO_2$/C catalyst (Fig. S52), respectively. The binding energies of $Ru_5$ clusters on the *m*-$ZrO_2$ and *t*-$ZrO_2$ surfaces were calculated separately to be − 6.75 and − 11.42 eV (Fig. S53), indicating favorable thermodynamic stability. In alkaline HER, the cleavage of the H–OH bond in $H_2O$ is inherently sluggish, limiting the overall reaction rate [76, 77]. To address this, we investigated $H_2O$ adsorption and subsequent dissociation at various sites on both catalysts, including Ru atoms within the $Ru_5$ clusters and neighboring Zr sites. Notably, the Zr atoms adjacent to the $Ru_5$ clusters exhibited stronger $H_2O$ adsorption (Fig. 5a), as indicated by more negative adsorption energies (− 0.83 and − 0.96 eV), compared to the Ru sites (− 0.63 and − 0.54 eV), which can be attributed to the *d*-band center ($\varepsilon_d$) of the Zr sites being closer to the Fermi level than that of the Ru sites according to the projected density of state (PDOS) result (Fig. S54). We further examined the subsequent dissociation of adsorbed $H_2O$ into *H and *OH on Zr sites (Fig. 5b). The results show that the energy barrier for water dissociation on the $Ru_5$/*m*-$ZrO_2$ catalyst is 0.28 eV, which is significantly lower than the barrier on $Ru_5$/*t*-$ZrO_2$ (0.89 eV), indicating that $Ru_5$/*m*-$ZrO_2$ possesses markedly enhanced catalytic activity for the cleavage of water molecules. Under realistic alkaline conditions where Zr sites undergo surface hydroxylation, we further evaluated water adsorption and

dissociation at the hydroxylated $Ru_5/m\text{-}ZrO_2$ interface. Compared to the non-hydroxylated surface, the hydroxylated surface exhibits enhanced water adsorption at the Zr site, with an adsorption energy of − 2.35 eV, and a lower dissociation barrier of 0.13 eV (Fig. S55). Thus, under operating conditions, the Zr site remains active, and its catalytic contribution is maintained or even enhanced.

In the HER process, the Gibbs free energy of H* adsorption ($\Delta G_{H^*}$) is commonly recognized as a key descriptor of a catalyst's hydrogen evolution activity [78]. Accordingly, we computed $\Delta G_{H^*}$ for the $Ru_5/m\text{-}ZrO_2$ and $Ru_5/t\text{-}ZrO_2$ catalysts, considering various adsorption sites, including each Ru atom within the $Ru_5$ cluster as well as Zr and O sites on the substrate (Fig. S56). Notably, our DFT results show that the $\Delta G_{H^*}$ at the top Ru site (Ru1) of the $Ru_5/m\text{-}ZrO_2$ catalyst was calculated to be − 0.06 eV (Fig. 5c), which is significantly lower than the lowest $\Delta G_{H^*}$ value on $Ru_5/t\text{-}ZrO_2$ (-0.38 eV), thermodynamically confirming that $Ru_5$ anchored on $m\text{-}ZrO_2$ exhibits superior HER performance. An in-depth inspection on the reaction pathway reveals that the departure of OH* on $m\text{-}ZrO_2$ as the potential-determining step (PDS) possesses a much lower free energy barrier (0.73 eV, Fig. 5d) with respect to $t\text{-}ZrO_2$ (1.25 eV, Fig. 5e). Moreover, the

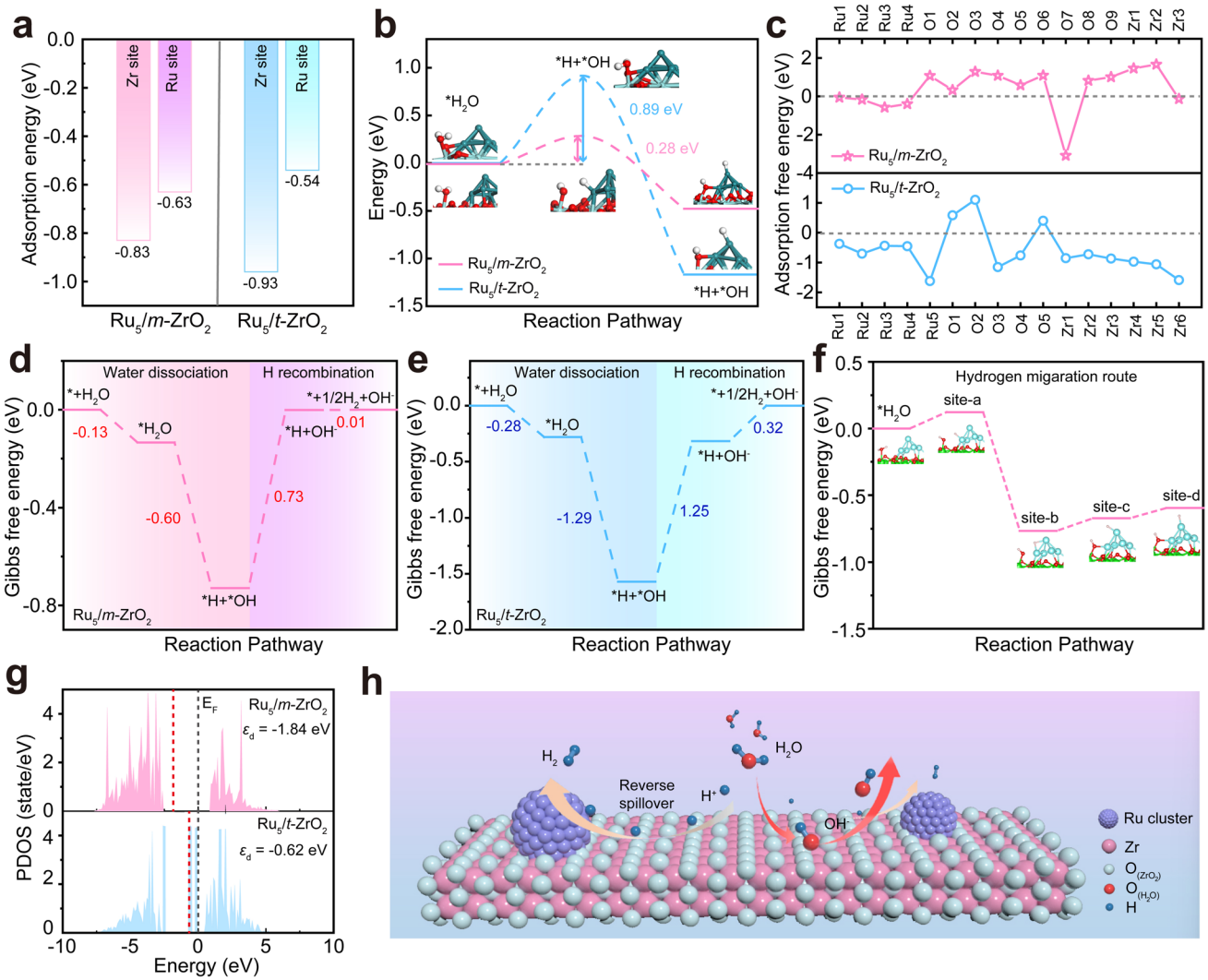


**Fig. 5** Theoretical calculation for HER mechanism. **a** Calculated $*H_2O$ adsorption energy on Zr and Ru sites in $Ru_5/m\text{-}ZrO_2$ and $Ru_5/t\text{-}ZrO_2$. **b** Kinetic energy barrier of $*H_2O$ dissociation on $Ru_5/m\text{-}ZrO_2$ and $Ru_5/t\text{-}ZrO_2$. **c** Hydrogen adsorption free energy ($\Delta G_{H^*}$) at Ru, Zr and O sites in $Ru_5/m\text{-}ZrO_2$ and $Ru_5/t\text{-}ZrO_2$. Gibbs free energy diagram for HER on **d** $Ru_5/m\text{-}ZrO_2$ and **e** $Ru_5/t\text{-}ZrO_2$. **f** Hydrogen migration energy on $Ru_5/m\text{-}ZrO_2$. **g** PDOS profiles of Ru *d* orbital for $Ru_5/m\text{-}ZrO_2$ and $Ru_5/t\text{-}ZrO_2$. **h** Schematic illustration of the HER mechanism


https://doi.org/10.1007/s40820-026-02289-3

generated active H* species preferentially spill over from the $m$-$ZrO_2$ support to the anchored $Ru_5$ cluster with a smaller thermodynamic barrier of 0.60 eV corresponding to an exergonic energy of 0.47 eV compared to $t$-$ZrO_2$ (thermodynamic barrier of 1.29 eV and exergonic energy of 1.17 eV), favoring the HRS process (Fig. 5f). The pronounced difference in H* adsorption strength between the $Ru_5$ clusters supported on $m$-$ZrO_2$ and $t$-$ZrO_2$ can be attributed to variations in the $\varepsilon_d$ of the Ru active sites (Fig. 5g). Specifically, the $\varepsilon_d$ of the Ru sites on the $m$-$ZrO_2$ surface lies further from the Fermi level (− 1.84 eV) than that on the $t$-$ZrO_2$ support (− 0.62 eV), resulting in weaker $H^*$ adsorption and bringing it closer to the ideal $\Delta G_{H^*}$ of 0 eV for optimal HER performance. Therefore, based on the above theoretical computations, we propose that the origin of the exceptional HER performance of $Ru_5$ clusters anchored on $ZrO_2$ lies in the differing work functions of the $Ru_5$ clusters and the $ZrO_2$ substrate (Fig. 2h), which leads to a significant accumulation of electrons at their interface and holds great promise for accelerating the OH* departure and hydrogen spillover process. Among the two materials, the $Ru_5$/$m$-$ZrO_2$ catalyst exhibits enhanced capability in facilitating the dissociation of adsorbed $H_2O$ molecules into OH* and H*, with a lower energy barrier of 0.28 eV, thereby promoting the spillover of $H^*$ species from the $m$-$ZrO_2$ support to the Ru cluster (Fig. 5h).

### 3.5 Practical Potential Application

Due to the growing scarcity of freshwater resources, direct seawater electrolysis for hydrogen production is increasingly imperative [79, 80]. In this context, we evaluated the HER performance of the Ru@$m$-$ZrO_2$/C catalyst in 1 M KOH with $x$ M NaCl ($x$ = 0. 0.5, 2) solution and alkaline simulated seawater (1 M KOH + simulated seawater) environments. As shown in Figs. 6a and S57, the catalyst exhibits slightly decreased HER activity in 1 M KOH + 2 M NaCl compared to pure 1 M KOH, yet still achieves a low overpotential of 42 mV at 10 mA $cm^{-2}$ and a Tafel slope of 33.3 mV $dec^{-1}$ (Fig. 6b), significantly outperforming Ru@$t$-$ZrO_2$/C, Pt/C, and Ru/C. To systematically assess chloride corrosion resistance, we tested the catalyst under varying $Cl^-$ concentrations ($x$ = 0, 0.5, 2 M NaCl in 1 M KOH), which reveals dramatically robust $Cl^-$ resistance capability (Fig. S58) [81, 82]. Furthermore, in situ XPS result indicated that the electronic structures of Ru and Zr retained intact after $Cl^-$ adsorption (Figs. S59 and S60). Besides, DFT calculated adsorption energies of $Cl^-$ range from − 1.47 to − 1.30 eV (Fig. S61), indicating spontaneous $Cl^-$ adsorption onto Ru active sites under experimental conditions. After $Cl^-$ adsorption, the $\Delta G_{H^*}$ at the top Ru site lies between − 0.01 and 0.06 eV, which is comparable to or even slightly better than that without $Cl^-$ (− 0.06 eV). Thus, $Cl^-$ adsorption does not adversely affect the intrinsic HER activity of the Ru sites. Chronopotentiometry tests at 20 mA $cm^{-2}$ for ~ 100 h further confirm the exceptional stability of Ru@$m$-$ZrO_2$/C in chloride-containing environments, demonstrating strong corrosion resistance (Figs. 6c and S63–S65, Table S14).

The HER performance of Ru@$m$-$ZrO_2$/C was further examined in a more realistic alkaline seawater system (1 M KOH + simulated seawater). Although the addition of KOH leads to precipitation of $Ca^{2+}$ and $Mg^{2+}$, which can block active sites [83], the catalyst requires an overpotential of only 30 mV to reach 10 mA $cm^{-2}$ (Figs. 6d and S62). This value is lower than those of Ru@$t$-$ZrO_2$/C (36 mV), Pt/C (42 mV), and Ru/C (47 mV) and ranks among the best reported catalysts (Table S14). Moreover, Ru@$m$-$ZrO_2$/C shows a Tafel slope of 62.9 mV $dec^{-1}$, superior to Ru@$t$-$ZrO_2$/C (69.7 mV $dec^{-1}$), Pt/C (112.0 mV $dec^{-1}$), and Ru/C (99.5 mV $dec^{-1}$), indicating favorable reaction kinetics in seawater electrolyte (Fig. 6e). The excellent stability of the catalyst in simulated seawater was further verified by chronopotentiometry at 20 mA $cm^{-2}$ for 100 h (Fig. 6f and Table S14). Post-stability characterization by XRD, Raman and SEM verified the structural integrity of Ru@$m$-$ZrO_2$/C (Figs. S63–S65). Furthermore, to assess potential surface blocking by $Ca^{2+}$ and $Mg^{2+}$ ions, XPS and TEM analyses were conducted on the tested samples. The results show that the Ru@$m$-$ZrO_2$/C maintained its structural stability after the test, with only minimal amounts of $Ca^{2+}$ and $Mg^{2+}$ ions detected (Figs. S66 and S67). Given its outstanding HER performance in both alkaline and seawater media, we assembled an AEMWE device using Ru@$m$-$ZrO_2$/C as the cathode and NiFe-LDH as the anode. Operating at 60 °C in 1 M KOH, the electrolyzer achieved current densities of 0.50, 1.0, and 2.0 A $cm^{-2}$ at cell voltages of 1.64, 1.76, and 1.98 V, respectively (Fig. 6g). These results surpass most

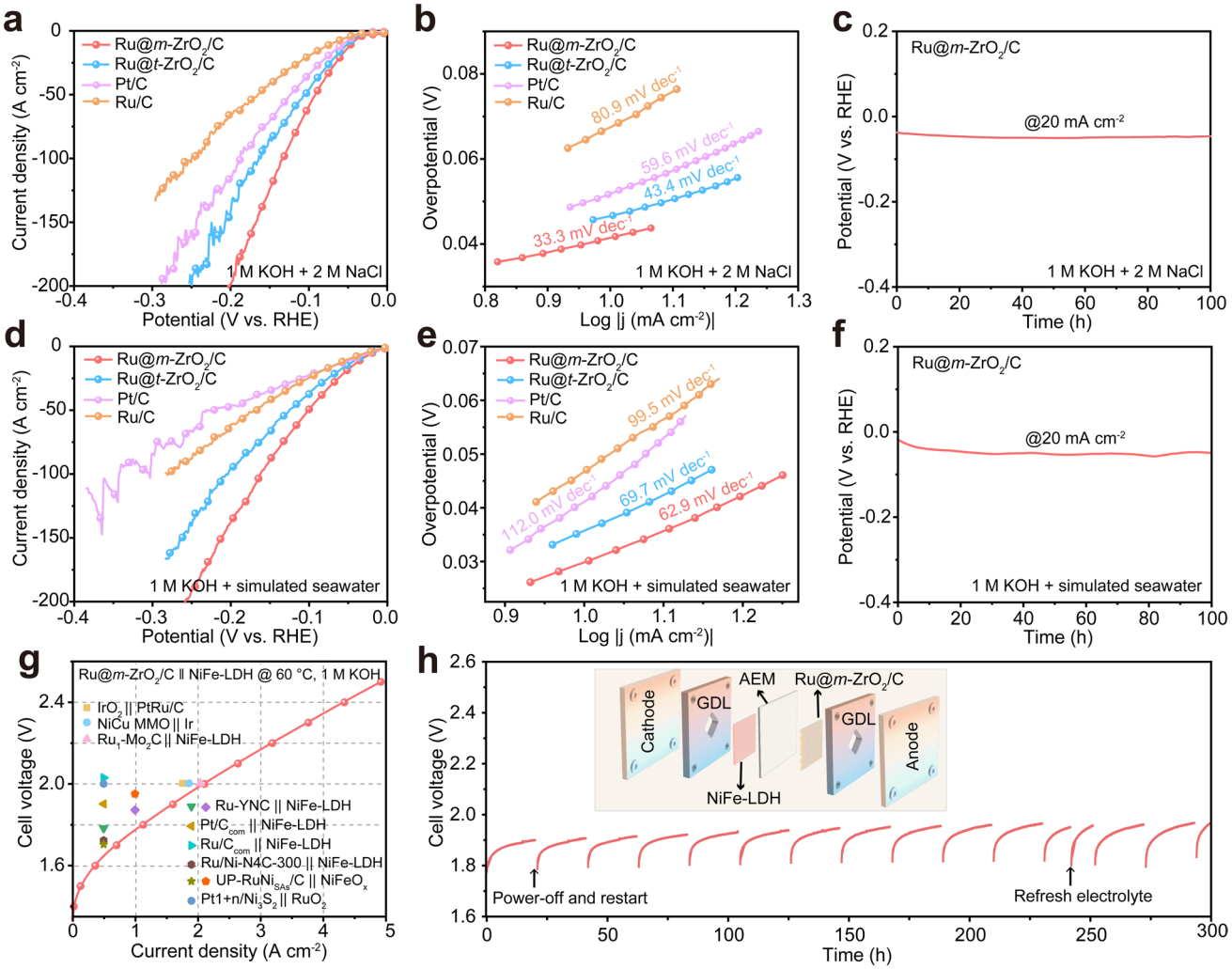


**Fig. 6** HER performance evaluation in practical application. **a** LSV polarization curves and **b** Tafel slopes measured in 1 M KOH + 2 M NaCl for Ru@*m*-$ZrO_2$/C, Ru@*t*-$ZrO_2$/C, Pt/C, and Ru/C, **c** the chronopotentiometry curve of Ru@*m*-$ZrO_2$/C in 1 M KOH + 2 M NaCl at 20 mA $cm^{-2}$. **d** LSV polarization curves and **e** Tafel slopes measured in 1 M KOH + simulated seawater for Ru@*m*-$ZrO_2$/C, Ru@*t*-$ZrO_2$/C, Pt/C and Ru/C, **f** the chronopotentiometry curve of Ru@*m*-$ZrO_2$/C in 1 M KOH + simulated seawater at 20 mA $cm^{-2}$. **g** Polarization curve of Ru@*m*-$ZrO_2$/C || NiFe-LDH based AEMWE device measured at 60 °C in 1 M KOH, inset showing a comparison with reported literatures. **h** Chronopotentiometry curve of the Ru@*m*-$ZrO_2$/C || NiFe-LDH device under a current density of 1 A $cm^{-2}$, inset showing a schematic illustration of the AEMWE device

reported electrocatalysts (Fig. 6g and Table S15). In view of the intermittent supply of renewable energy (solar, wind, *etc.*), the catalyst stability was studied by simulating the frequent start–stop operation cycles of water electrolysis. The system demonstrated remarkable stability, maintaining operation at an industrial-level current density of 1 A $cm^{-2}$ for more than 300 h (Fig. 6h), highlighting its potential for practical high-current–density water electrolysis and commercial application.

## 4 Conclusions

In summary, this work establishes that the crystal phase of $ZrO_2$ significantly influences the electronic metal–support interaction and hydrogen reverse spillover process, thereby dictating the HER performance of Ru nanoclusters. In situ Raman and EIS analysis revealed the enhanced interfacial water activation and dissociation process on *m*-$ZrO_2$. DFT calculations further unveiled that work function-induced


https://doi.org/10.1007/s40820-026-02289-3

charge accumulation at the Ru/*m*-$ZrO_2$ interface facilitates water adsorption and dissociation at Zr sites and accelerates reverse hydrogen spillover from the *m*-$ZrO_2$ substrate to Ru sites by regulating the *d*-band center of Ru, thereby enhancing electrocatalytic HER performance. These fundamental insights, coupled with the exceptional catalytic performance—exemplified by an overpotential of 28 mV in 1 M KOH and 30 mV in alkaline seawater at 10 mA $cm^{-2}$, and stable AEMWE performance at industrial current density for more than 300 h—demonstrate the great potential of phase-engineered supports in designing highly efficient and durable electrocatalysts for renewable hydrogen production.

**Acknowledgements** This work was supported by the Scientific Research Innovation Capability Support Project for Young Faculty (SRICSPYF-BS2025053), National Natural Science Foundation of China (No. 52572048, U22A20144, 52572110), Shaanxi Provincial Education Department Science and Technology (24JR032), Science and Technology Program of Weiyang District of Xi'an, China (202315, 202401), Shaanxi Key Laboratory of Green Preparation and Functionalization for Inorganic Materials (SKL002), and the National Research Foundation Singapore, and A*STAR (Agency for Science, Technology and Research) under its LCER Phase 2 Programme 1st Emerging Technology (Award No. U2411D4006) and Key Laboratory of Functional Inorganic Material Chemistry (Heilongjiang University), Ministry of Education, P. R. China.

**Author Contributions** Jun Zhang involved in writing—original draft. Xiaoyu Chen, Bin Wu, and Xiangyang Guo took part in formal analysis. Xianlin Qu, Yi Wang, Qunzhi Ma, Ying Wang, Jiayi Li, Wei Liu, and Xu Li involved in investigation. Jianfeng Huang and Liyun Cao took part in supervision. Jingxiang Zhao, Fuxiang Zhang, and Yongqiang Feng carried out writing—review and editing. Yongqiang Feng and Bin Wu involved in conceptualization, methodology. All authors participated in reviewing and editing the final manuscript.

**Declarations**

**Conflict of interest** The authors declare no interest conflict. They have no known conflict of financial interest or personal relationships that could have appeared to influence the work reported in this paper.



**Supplementary Information** The online version contains supplementary material available at https://doi.org/10.1007/s40820-026-02289-3.

## References

1. Q. Yun, Y. Ge, Z. Shi, J. Liu, X. Wang et al., Recent progress on phase engineering of nanomaterials. Chem. Rev. **123**(23), 13489–13692 (2023). https://doi.org/10.1021/acs.chemrev.3c00459
2. X. Xu, H.C. Chen, L. Li, M. Humayun, X. Zhang et al., Leveraging metal nodes in metal-organic frameworks for advanced anodic hydrazine oxidation assisted seawater splitting. ACS Nano **17**(11), 10906–10917 (2023). https://doi.org/10.1021/acsnano.3c02749
3. Y.Y. Ge, X.X. Wang, B. Chen, Z.Q. Huang, Z.Y. Shi et al., Preparation of *fcc*-2H-*fcc* heterophase Pd@Ir nanostructures for high-performance electrochemical hydrogen evolution. Adv. Mater. **34**(4), 2107399 (2022). https://doi.org/10.1002/adma.202107399
4. H.J. Wang, Y. Qin, Y. Wu, Y.W. Qiu, L. Ling et al., Pd hydride metallene aerogels with lattice hydrogen participation for efficient hydrogen evolution reaction. Nat. Commun. **15**(1), 10289 (2024). https://doi.org/10.1038/s41467-024-54601-7
5. F.M. Wang, L. Ju, B.L. Wu, S.H. Li, J. Peng et al., Effect of intrinsic ferroelectric phase transition on hydrogen evolution electrocatalysis. Angew. Chem. Int. Ed. **63**(18), e202402033 (2024). https://doi.org/10.1002/anie.202402033
6. Q.Z. Gao, X.L. Zheng, J.X. Lin, J.D. Zhai, F. Yang et al., Design concept of metal sulfide photocatalyst for efficient photocatalytic hydrogen evolution. Nano-Micro Lett. **18**(1), 266 (2026). https://doi.org/10.1007/s40820-026-02111-0
7. J. Jin, X.Y. Wang, Y. Hu, Z. Zhang, H.B. Liu et al., Precisely control relationship between sulfur vacancy and H absorption for boosting hydrogen evolution reaction. Nano-Micro Lett. **16**(1), 63 (2024). https://doi.org/10.1007/s40820-023-01291-3
8. X.L. Zhang, P.C. Yu, X.Z. Su, S.J. Hu, L. Shi et al., Efficient acidic hydrogen evolution in proton exchange membrane electrolyzers over a sulfur-doped marcasite-type electrocatalyst. Sci. Adv. **9**(27), eadh2885 (2023). https://doi.org/10.1126/sciadv.adh2885
9. X.L. Zhang, P.C. Yu, S.P. Sun, L. Shi, P.P. Yang et al., In situ ammonium formation mediates efficient hydrogen production from natural seawater splitting. Nat. Commun. **15**(1), 9462 (2024). https://doi.org/10.1038/s41467-024-53724-1
10. X. Zhu, Y.C. Wang, K. Qu, L. Song, J. Wang et al., Modulating Ru-Co bond lengths in $Ru_1$ Co single-atom alloys through crystal phase engineering for electrocatalytic nitrate-to-ammonia conversion. Nat. Commun. **16**(1), 5742 (2025). https://doi.org/10.1038/s41467-025-61232-z

11. Z.H. Yuan, B. Sun, W. Zhong, X. Ai, J.Z. Gao et al., Architecture engineering and phase engineering of rhodium metallene Co-boost nitrite-to-ammonia electroconversion. Angew. Chem. Int. Ed. **64**(40), e202509944 (2025). https://doi.org/10.1002/ange.202509944
12. X. Zhang, L. Hui, F. He, Y. Li, The interfacial interpenetration effect for controlled reaction stability of palladium catalysts. J. Am. Chem. Soc. **147**(1), 436–445 (2025). https://doi.org/10.1021/jacs.4c11234
13. X. Zhou, Y. Ma, Y. Ge, S. Zhu, Y. Cui et al., Preparation of Au@Pd core-shell nanorods with *fcc*-2H-*fcc* heterophase for highly efficient electrocatalytic alcohol oxidation. J. Am. Chem. Soc. **144**(1), 547–555 (2022). https://doi.org/10.1021/jacs.1c11313
14. S.Q. Xie, J.S. Fu, Q. Huang, W.H. Yang, A. Yu et al., Electronic modulation and active site exposure using $C_{60}$ fullerenolamine enable high-performance alcohol oxidation on Pd metallene catalysts. Angew. Chem. Int. Ed. **64**(32), e202506044 (2025). https://doi.org/10.1002/anie.202506044
15. Y. Wang, J. Wang, J. Xu, X. Qu, L. Lin et al., Fullerene-buffered electron shuttle of Ru/$RuO_2$ with switchable active sites enables robust and efficient bifunctional alkaline water electrolysis. Angew. Chem. Int. Ed. **64**(23), e202503608 (2025). https://doi.org/10.1002/anie.202503608
16. Q. Hu, K. Gao, X. Wang, H. Zheng, J. Cao et al., Subnanometric Ru clusters with upshifted D band center improve performance for alkaline hydrogen evolution reaction. Nat. Commun. **13**(1), 3958 (2022). https://doi.org/10.1038/s41467-022-31660-2
17. Y. Liu, Y. Wang, P. Fornasiero, G. Tian, P. Strasser et al., Long-term durability of seawater electrolysis for hydrogen: From catalysts to systems. Angew. Chem. Int. Ed. **63**(47), e202412087 (2024). https://doi.org/10.1002/anie.202412087
18. J.W. Zhu, X.F. Lu, D.Y. Luan, X.W. Lou, Metal-organic frameworks derived carbon-supported metal electrocatalysts for energy-related reduction reactions. Angew. Chem. Int. Ed. **63**(38), e202408846 (2024). https://doi.org/10.1002/anie.202408846
19. L. Zong, F. Lu, P. Li, K. Fan, T. Zhan et al., Thermal shock synthesis for loading Sub-2 nm Ru nanoclusters on titanium nitride as a remarkable electrocatalyst toward hydrogen evolution reaction. Adv. Mater. **36**(32), e2403525 (2024). https://doi.org/10.1002/adma.202403525
20. T. Luo, J. Huang, Y. Hu, C. Yuan, J. Chen et al., Fullerene lattice-confined Ru nanoparticles and single atoms synergistically boost electrocatalytic hydrogen evolution reaction. Adv. Funct. Mater. **33**(12), 2213058 (2023). https://doi.org/10.1002/adfm.202213058
21. K. Liu, Y.H. Cai, X.T. Wei, L.H. Qu, J.X. Lu et al., Dual chloride confinement in noble metal-doped NiV LDH catalysts enables stable industrial-level seawater electrolysis. Nano-Micro Lett. **18**(1), 210 (2026). https://doi.org/10.1007/s40820-026-02067-1
22. Y. Liu, G. Liu, X.Y. Chen, C. Xue, M.K. Sun et al., Achieving negatively charged Pt single atoms on amorphous $Ni(OH)_2$ nanosheets with promoted hydrogen absorption in hydrogen evolution. Nano-Micro Lett. **16**(1), 202 (2024). https://doi.org/10.1007/s40820-024-01420-6
23. M. Zhao, Z. Chen, Z. Lyu, Z.D. Hood, M. Xie et al., Ru octahedral nanocrystals with a face-centered cubic structure, {111} facets, thermal stability up to 400 °C, and enhanced catalytic activity. J. Am. Chem. Soc. **141**(17), 7028–7036 (2019). https://doi.org/10.1021/jacs.9b01640
24. Z.Y. Shi, X. Zhang, X.Q. Lin, G.G. Liu, C.Y. Ling et al., Phase-dependent growth of Pt on $MoS_2$ for highly efficient $H_2$ evolution. Nature **621**(7978), 300–305 (2023). https://doi.org/10.1038/s41586-023-06339-3
25. J. Dai, Y. Zhu, Y. Chen, X. Wen, M. Long et al., Hydrogen spillover in complex oxide multifunctional sites improves acidic hydrogen evolution electrocatalysis. Nat. Commun. **13**(1), 1189 (2022). https://doi.org/10.1038/s41467-022-28843-2
26. J. Li, J. Hu, M. Zhang, W. Gou, S. Zhang et al., A fundamental viewpoint on the hydrogen spillover phenomenon of electrocatalytic hydrogen evolution. Nat. Commun. **12**(1), 3502 (2021). https://doi.org/10.1038/s41467-021-23750-4
27. Y. Feng, Y. Wei, B. Wu, J.N. Li, Q. Dong et al., Tuning D-band electronic interaction between Pt and Ru confined in fullerene network accelerate hydrogen spillover for efficient and pH-universal hydrogen evolution. Adv. Energy Mater. **15**(40), e03878 (2025). https://doi.org/10.1002/aenm.202503878
28. J. Chen, C. Chen, M. Qin, B. Li, B. Lin et al., Reversible hydrogen spillover in Ru-$Wo_{3-x}$ enhances hydrogen evolution activity in neutral pH water splitting. Nat. Commun. **13**(1), 5382 (2022). https://doi.org/10.1038/s41467-022-33007-3
29. W. Shao, Z. Xing, X. Xu, D. Ye, R. Yan et al., Bioinspired proton pump on ferroelectric $HfO_2$-coupled Ir catalysts with bidirectional hydrogen spillover for pH-universal and superior hydrogen production. J. Am. Chem. Soc. **146**(40), 27486–27498 (2024). https://doi.org/10.1021/jacs.4c08100
30. C. Yue, G. Sun, N. Liu, W. Bao, X. Zhang et al., Lattice-confined Pt-Ru dual-atom pair by space guard for robust hydrogen evolution with reversible hydrogen spillover. Adv. Energy Mater. **15**(39), e02578 (2025). https://doi.org/10.1002/aenm.202502578
31. C. Xu, H. Yu, H. Huang, S. Li, Y. Cao et al., Hydroxyl spillover activated from the strongly coupled Ru@$Mn_3O_4$ heterostructure to promote alkaline hydrogen evolution. Angew. Chem. Int. Ed. **64**(37), e202504667 (2025). https://doi.org/10.1002/anie.202504667
32. X.Q. Gao, Y.T. Chen, Y.J. Wang, L.Y. Zhao, X.Y. Zhao et al., Next-generation green hydrogen: progress and perspective from electricity, catalyst to electrolyte in electrocatalytic water splitting. Nano-Micro Lett. **16**(1), 237 (2024). https://doi.org/10.1007/s40820-024-01424-2
33. X.Q. You, D.A. Zhang, X.G. Zhang, X.Y. Li, J.H. Tian et al., Exploring the cation regulation mechanism for interfacial water involved in the hydrogen evolution reaction by in situ Raman spectroscopy. Nano-Micro Lett. **16**(1), 53 (2024). https://doi.org/10.1007/s40820-023-01285-1
34. Z. Yang, J. Zhang, X. Tan, H. Zhu, L. Xu et al., Manipulating the coordination environment of Cu single atoms via


 https://doi.org/10.1007/s40820-026-02289-3

regulating $ZrO_2$ support crystal phases for enhanced $CO_2$ electroreduction. J. Am. Chem. Soc. **147**(39), 35985–35994 (2025). https://doi.org/10.1021/jacs.5c13661

35. A.P. Solomon, E.C. O'Quinn, J.J. Liu, I.M. Gussev, X.F. Guo et al., Atomic-scale structure of $ZrO_2$: formation of metastable polymorphs. Sci. Adv. **11**(1), adq5943 (2025). https://doi.org/10.1126/sciadv.adq5943
36. T.R. Wang, J.Y. Hu, R.H. Ouyang, Y.T. Wang, Y. Huang et al., Nature of metal-support interaction for metal catalysts on oxide supports. Science **386**(6724), 915–920 (2024). https://doi.org/10.1126/science.adp6034
37. Z.J. Lin, N. Sathishkumar, Y. Xia, S.Z. Li, X. Liu et al., Tailoring zirconia supported intermetallic platinum alloy via reactive metal-support interactions for high-performing fuel cells. Angew. Chem. Int. Ed. **63**(26), e202400751 (2024). https://doi.org/10.1002/anie.202400751
38. M. Kim, S.H. Kim, J. Park, S.S. Lee, I. Jang et al., Reconstructing oxygen-deficient zirconia with ruthenium catalyst on atomic-scale interfaces toward hydrogen production. Adv. Funct. Mater. **33**(29), 2300673 (2023). https://doi.org/10.1002/adfm.202300673
39. S.R. Fang, H.X. Yang, H.Y. Lin, M.Y. Lin, F.X. Mao et al., Tetragonal $ZrO_2$ supported low-iridium catalyst activating oxygen spillover stabilized lattice oxygen for proton exchange membrane water electrolysis. Energy Environ. Sci. **18**(11), 5470–5481 (2025). https://doi.org/10.1039/d5ee00544b
40. M.J. Katz, Z.J. Brown, Y.J. Colon, P.W. Siu, K.A. Scheidt et al., A facile synthesis of UiO-66, UiO-67 and their derivatives. Chem. Commun. **49**(82), 9449–9451 (2013). https://doi.org/10.1039/c3cc46105j
41. J.H. Cavka, S. Jakobsen, U. Olsbye, N. Guillou, C. Lamberti et al., A new zirconium inorganic building brick forming metal organic frameworks with exceptional stability. J. Am. Chem. Soc. **130**(42), 13850–13851 (2008). https://doi.org/10.1021/ja8057953
42. H. Sun, H.C. Chen, M. Humayun, Y. Qiu, J. Ju et al., Unlocking the catalytic potential of platinum single atoms for industry-level current density chlorine tolerance hydrogen generation. Adv. Funct. Mater. **34**(49), 2408872 (2024). https://doi.org/10.1002/adfm.202408872
43. Y. Wei, M. Gao, X. Huo, W. Zhu, Q. Liu et al., Defect-rich CoRu alloy embedded in the porous carbon serving as highly-efficient and bifunctional electrocatalyst for overall water splitting over a wide pH range. Chem. Eng. J. **492**, 152337 (2024). https://doi.org/10.1016/j.cej.2024.152337
44. Y. Feng, W. Feng, J. Wan, J. Chen, H. Wang et al., Appl. Catal. B-Environ. **307**, 121193 (2022). https://doi.org/10.1016/j.apcatb.2022.121193
45. J.N. Hansen, H. Prats, K.K. Toudahl, NMørch. Secher, K. Chan et al., Is there anything better than Pt for HER? ACS Energy Lett. **6**(4), 1175–1180 (2021). https://doi.org/10.1021/acsenergylett.1c00246
46. G. Kresse, D. Joubert, Projector augmented-wave pseudopotentials for uranium-based compounds. Phys. Rev. B **59**, 1758–1775 (1999). https://doi.org/10.1016/j.commatsci.2019.109237
47. J.P. Perdew, K. Burke, M. Ernzerhof, Generalized gradient approximation made simple. Phys. Rev. Lett. **77**, 3865–3868 (1996). https://doi.org/10.1103/PhysRevLett.77.3865
48. P.E. Blochl, O. Jepsen, O.K. Andersen, Improved tetrahedron method for Brillouin-zone integrations. Phys. Rev. B **49**(23), 16223–16233 (1994). https://doi.org/10.1103/physrevb.49.16223
49. S. Maintz, V.L. Deringer, A.L. Tchougreeff, R. Dronskowski, Lobster: a tool to extract chemical bonding from plane-wave based DFT. J. Comput. Chem. **37**(11), 1030–1035 (2016). https://doi.org/10.1002/jcc.24300
50. G. Henkelman, B.P. Uberuaga, H. Jónsson, A climbing image nudged elastic band method for finding saddle points and minimum energy paths. J. Chem. Phys. **113**(22), 9901–9904 (2000). https://doi.org/10.1063/1.1329672
51. N. Turaeva, G. Yablonsky, R. Fushimi, Fermi-based kinetic model for the Sabatier reaction: Sabatier principle and beyond it. J. Phys. Chem. C **129**(16), 7730–7739 (2025). https://doi.org/10.1021/acs.jpcc.5c00099
52. F. Podjaski, D. Weber, S.Y. Zhang, L. Diehl, R. Eger et al., Rational strain engineering in delafossite oxides for highly efficient hydrogen evolution catalysis in acidic media. Nat. Catal. **3**(1), 55–63 (2020). https://doi.org/10.1038/s41929-019-0400-x
53. W. Chen, W. Wei, F. Li, Y. Wang, M. Liu et al., Tunable built-in electric field in Ru nanoclusters-based electrocatalyst boosts water splitting and simulated seawater electrolysis. Adv. Funct. Mater. **34**(7), 2310690 (2023). https://doi.org/10.1002/adfm.202310690
54. T. Xiao, X. Liu, G. Xu, Y. Zhang, Phase tuning of $ZrO_2$ supported cobalt catalysts for hydrodeoxygenation of 5-hydroxymethylfurfural to 2,5-dimethylfuran under mild conditions. Appl. Catal. B Environ. **295**, 120270 (2021). https://doi.org/10.1016/j.apcatb.2021.120270
55. J. Cheng, J. Xie, Y. Xi, X. Wu, R. Zhang et al., Selective upcycling of polyethylene terephthalate towards high-valued oxygenated chemical methyl p-methyl benzoate using a Cu/$ZrO_2$ catalyst. Angew. Chem. Int. Ed. **63**(11), e202319896 (2024). https://doi.org/10.1002/anie.202319896
56. C. Yang, C. Pei, R. Luo, S. Liu, Y. Wang et al., Strong electronic oxide-support interaction over $In_2O_3$/ $ZrO_2$ for highly selective $CO_2$ hydrogenation to methanol. J. Am. Chem. Soc. **142**(46), 19523–19531 (2020). https://doi.org/10.1021/jacs.0c07195
57. X. Mu, X. Zhang, Z. Chen, Y. Gao, M. Yu et al., Constructing symmetry-mismatched $Ru_xFe_{3-x}O_4$ heterointerface-supported Ru clusters for efficient hydrogen evolution and oxidation reactions. Nano Lett. **24**(3), 1015–1023 (2024). https://doi.org/10.1021/acs.nanolett.3c04690
58. F. Meneghetti, E. Wendel, S. Mascotto, B.M. Smarsly, E. Tondello et al., Combined use of XAFS, XRD and TEM to unravel the microstructural evolution of nanostructured $ZrO_2$–$SiO_2$ binary oxides: from nanometres down to the

molecular domain. CrystEngComm **12**(5), 1639–1649 (2010). https://doi.org/10.1039/b911004f

59. M. Yang, J. Yu, A. Zimina, B.B. Sarma, J.D. Grunwaldt et al., Unlocking a dual-channel pathway in $CO_2$ hydrogenation to methanol over single-site zirconium on amorphous silica. Angew. Chem. Int. Ed. **63**(4), e202312292 (2024). https://doi.org/10.1002/anie.202312292
60. M.N. Li, G.H. Huang, X.J. Chen, Z.Y. Xu, J. Huang et al., Development of an EOR-produced petroleum wastewater treatment system through integrated polyacrylonitrile membrane and $ZrO_2$ sericin technologies: revelation of interactive mechanism based on synchrotron and XDLVO analyses. NPJ Clean Water **8**(1), 24 (2025). https://doi.org/10.1038/s41545-025-00454-6
61. D. Salusso, E. Borfecchia, S. Bordiga, Combining X-ray diffraction and X-ray absorption spectroscopy to unveil Zn local environment in Zn-doped $ZrO_2$ catalysts. J. Phys. Chem. C **125**(40), 22249–22261 (2021). https://doi.org/10.1021/acs.jpcc.1c06202
62. H. Zeng, Z. Chen, Q. Jiang, Q. Zhong, Y. Ji et al., Sustainable and cost-efficient hydrogen production using platinum clusters at minimal loading. Nat. Commun. **16**(1), 4314 (2025). https://doi.org/10.1038/s41467-025-59450-6
63. H. Song, M. Wu, Z. Tang, J.S. Tse, B. Yang et al., Single atom ruthenium-doped CoP/CDs nanosheets via splicing of carbon-dots for robust hydrogen production. Angew. Chem. Int. Ed. **60**(13), 7234–7244 (2021). https://doi.org/10.1002/anie.202017102
64. K. Chen, Z. Liu, S. Zhu, Y. Liu, Y. Liu et al., Ruthenium-nickel nanoparticles with unconventional face-centered cubic crystal phase for highly active electrocatalytic hydrogen evolution. Adv. Funct. Mater. **34**(44), 2406259 (2024). https://doi.org/10.1002/adfm.202406259
65. J. Gu, L. Chen, J. Zhang, C. Zhang, J. Li et al., Metastable phase engineering of core@shell RuFe@Ru for boosting hydrogen evolution. Nano Lett. **25**(24), 9872–9879 (2025). https://doi.org/10.1021/acs.nanolett.5c02375
66. C. Yang, Z. Wu, Z. Zhao, Y. Gao, T. Ma et al., Electronic structure-dependent water-dissociation pathways of ruthenium-based catalysts in alkaline $H_2$-evolution. Small **19**(14), e2206949 (2023). https://doi.org/10.1002/smll.202206949
67. M. Wang, Z. Shi, W. Shi, J. Jiang, J. Lan et al., Ultrafast H-spillover in intermetallic PtZn induced by the local disorder for excellent electrocatalytic hydrogen evolution performance. Adv. Mater. **37**(3), e2409575 (2025). https://doi.org/10.1002/adma.202409575
68. J. Zhang, L. Zhang, J. Liu, C. Zhong, Y. Tu et al., OH spectator at IrMo intermetallic narrowing activity gap between alkaline and acidic hydrogen evolution reaction. Nat. Commun. **13**(1), 5497 (2022). https://doi.org/10.1038/s41467-022-33216-w
69. D. Li, M. Chen, D. Liu, C. Shen, H. Sun et al., Engineering ruthenium species on metal-organic frameworks for water electrolysis at industrial current densities. Adv. Energy Mater. **15**(15), 2404714 (2024). https://doi.org/10.1002/aenm.202404714
70. X. Chen, X.T. Wang, J.B. Le, S.M. Li, X. Wang et al., Revealing the role of interfacial water and key intermediates at ruthenium surfaces in the alkaline hydrogen evolution reaction. Nat. Commun. **14**(1), 5289 (2023). https://doi.org/10.1038/s41467-023-41030-1
71. Y. Feng, W. Zhu, J. Xu, D. Zhang, Q. Ma et al., Steering the electronic microenvironment of ruthenium sites via boron buffering enables enhanced hydrogen evolution under a universal pH range. ACS Nano **19**(8), 7948–7961 (2025). https://doi.org/10.1021/acsnano.4c14866
72. Y.H. Wang, S. Zheng, W.M. Yang, R.Y. Zhou, Q.F. He et al., In situ Raman spectroscopy reveals the structure and dissociation of interfacial water. Nature **600**(7887), 81–85 (2021). https://doi.org/10.1038/s41586-021-04068-z
73. H. Fan, Q.Q. Yang, S.R. Fang, Y.N. Xu, Y. Lv et al., Operando stable palladium hydride nanoclusters anchored on tungsten carbides mediate reverse hydrogen spillover for hydrogen evolution. Angew. Chem. Int. Ed. **63**(51), e202412080 (2024). https://doi.org/10.1002/anie.202412080
74. P. Yan, T. Yang, M. Lin, Y. Guo, Z. Qi et al., "One stone five birds" plasma activation strategy synergistic with Ru single atoms doping boosting the hydrogen evolution performance of metal hydroxide. Adv. Funct. Mater. **33**(25), 2301343 (2023). https://doi.org/10.1002/adfm.202301343
75. W. Li, F. Li, H. Yang, X. Wu, P. Zhang et al., A bio-inspired coordination polymer as outstanding water oxidation catalyst via second coordination sphere engineering. Nat. Commun. **10**(1), 5074 (2019). https://doi.org/10.1038/s41467-019-13052-1
76. C.A. Zhou, K. Ma, Z. Zhuang, M. Ran, G. Shu et al., Tuning the local environment of pt species at CNT@$Mo_{(2-x)}$ (m = Sn and Ce) heterointerfaces for boosted alkaline hydrogen evolution. J. Am. Chem. Soc. **146**(31), 21453–21465 (2024). https://doi.org/10.1021/jacs.4c04189
77. H.D. Wang, Y.X. Jiao, G.H. Zhang, W.C. Ma, W.J. Fan et al., Stabilizing electron-deficient Ru nanoclusters via strong electronic metal-support interaction for practical anion-exchange membrane electrolyzer. Adv. Funct. Mater. **35**(14), 2418617 (2025). https://doi.org/10.1002/adfm.202418617
78. K. Jiang, B. Liu, M. Luo, S. Ning, M. Peng et al., Single platinum atoms embedded in nanoporous cobalt selenide as electrocatalyst for accelerating hydrogen evolution reaction. Nat. Commun. **10**(1), 1743 (2019). https://doi.org/10.1038/s41467-019-09765-y
79. L. Yu, M.H. Ning, Y. Wang, C.Q. Yuan, Z.F. Ren, Direct seawater electrolysis for hydrogen production. Nat. Rev. Mater. **10**, 857–873 (2025). https://doi.org/10.1038/s41578-025-00826-x
80. S. Liu, Z. Zhang, K. Dastafkan, Y. Shen, C. Zhao et al., Yttrium-doped NiMo-$MoO_2$ heterostructure electrocatalysts for hydrogen production from alkaline seawater. Nat. Commun. **16**(1), 773 (2025). https://doi.org/10.1038/s41467-025-55856-4
81. W. Ma, X. Yang, D. Li, R. Xu, L. Nie et al., Ru-W pair sites enabling the ensemble catalysis for efficient hydrogen

 https://doi.org/10.1007/s40820-026-02289-3

evolution. Adv. Sci. **10**(26), e2303110 (2023). https://doi.org/10.1002/advs.202303110

82. X. Zhao, H. Zheng, H. Sun, M. Chen, B. Wang et al., Interfacial component coupling effects induce electron redistribution for enhanced hydrazine-assisted hydrogen production at ampere-level current densities. Nano Energy **142**, 111201 (2025). https://doi.org/10.1016/j.nanoen.2025.111201
83. J. Zhao, J. Wang, J. Yao, L. Li, D. Chen et al., Delicate control over electron distribution and water dissociation kinetics in strongly coupled Ru@NMoC hybrid catalyst realizes efficient seawater electrolysis. Angew. Chem. Int. Ed. **64**(30), e202505031 (2025). https://doi.org/10.1002/anie.202505031